

Red Supergiant Stars within the Local Group

Lee. R. Patrick



Doctor of Philosophy
The University of Edinburgh
March 2016

Chapter 1

KMOS Observations in NGC 6822

1.1 Introduction

A promising new method to directly probe chemical abundances in external galaxies is with J -band spectroscopy of red supergiant (RSG) stars. With their peak flux at $\sim 1\,\mu\text{m}$ and luminosities in excess of $10^4\,\text{L}_\odot$, RSGs are extremely bright in the near-IR, making them potentially useful tracers of the chemical abundances of star-forming galaxies out to large distances. To realise this goal, ? outlined a technique to derive metallicities of RSGs at moderate spectral resolving power ($R \sim 3000$). This technique has recently been refined using observations of RSGs in the Magellanic Clouds (?) and Perseus OB-1 (?). Using absorption lines in the J -band from iron, silicon and titanium, one can estimate metallicity ($[Z] = \log Z/Z_\odot$) as well as other stellar parameters (effective temperature, surface gravity and microturbulence) by fitting synthetic spectra to the observations. Owing to their intrinsic brightness, RSGs are ideal candidates for studies of extragalactic environments in the near-IR.

To make full use of the potential of RSGs for this science, multi-object spectrographs operating in the near-IR on 8-m class telescopes are essential. These instruments allow us to observe a large sample of RSGs in a given galaxy, at a wavelength where RSGs are brightest. In this context, the K -band Multi-Object Spectrograph (KMOS; ?) at the Very Large Telescope (VLT), Chile, is a powerful facility. KMOS will enable determination of stellar abundances for RSGs out to distances of $\sim 10\,\text{Mpc}$. Further ahead, a near-IR multi-object spectrograph on

a 40-m class telescope, combined with the excellent image quality from adaptive optics, will enable abundance estimates for individual stars in galaxies out to tens of Mpc, a significant volume of the local universe containing entire galaxy clusters (?).

Here we present KMOS observations of RSGs in the dwarf irregular galaxy NGC 6822, at a distance of ~ 0.46 Mpc (?), and references therein). Chemical abundances have been determined for its old stellar population (e.g. ??), but knowledge of its recent chemical evolution and present-day abundances is somewhat limited. Observations of two A-type supergiants by ? provided a first estimate of stellar abundances, finding $\log(\text{Fe/H}) + 12 = 7.01 \pm 0.22$ and $\log(\text{O/H}) + 12 = 8.36 \pm 0.19$, based on line-formation calculations for these elements assuming local thermodynamic equilibrium (LTE). A detailed non-LTE study for one of these objects confirmed the results finding 6.96 ± 0.09 for iron and 8.30 ± 0.02 for oxygen (?). Compared to solar values of 7.50 and 8.69, respectively (?), this indicates abundances that are approximately one third solar in NGC 6822. A study of oxygen abundances in H II regions (?) found a value of 8.11 ± 0.1 , confirming the low metallicity.

NGC 6822 is a relatively isolated Local Group galaxy, which does not seem to be associated with either M31 or the Milky Way. It appears to have a large extended stellar halo (??) as well as an extended HI disk containing tidal arms and a possible HI companion (?). The HI disk is orientated perpendicular to the distribution of old halo stars and has an associated population of blue stars (??). This led ? to label the system as a “polar ring galaxy”. A population of remote star clusters aligned with the elongated old stellar halo have been discovered (??). In summary, the extended structures of NGC 6822 suggest some form of recent interaction.

In addition, there is evidence for a relatively constant star-formation history within the central 5 kpc (?) with multiple stellar populations (??). This includes evidence for recent star formation in the form of a known population of massive stars, as well as a number of H II regions (????).

In this chapter I present near-IR KMOS spectroscopy of RSGs in NGC 6822 to investigate their chemical abundances. In Section 1.2 the details of the observations are described. Section 1.3 describes the data reduction and Section 1.4 details the derived stellar parameters and investigates the spatial distribution of the estimated metallicities in NGC 6822. A discussion of the key

results is presented in Section 1.5 and Section 1.6 concludes the chapter.

1.2 Observations

1.2.1 Target Selection

Targets were selected from optical photometry (?), combined with near-IR (JHK_s) photometry (for details see ?) from the Wide-Field Camera (WFCAM) on the United Kingdom Infra-Red Telescope (UKIRT). The two catalogues were cross-matched and only sources classified as stellar in the photometry for all filters were considered.

Our spectroscopic targets were selected principally based on their optical colours, as defined by ? and ?. Figure 1.1 shows cross-matched stars, with the dividing line at $(B - V) = 1.25 \times (V - R) + 0.45$. All stars redder than this line, above a given magnitude threshold and with $V - R > 0.6$, are potential RSGs.

Distinguishing between RSGs and the most luminous stars on the asymptotic giant branch (AGB) is difficult owing to their similar temperatures and overlapping luminosities. Near-IR photometry can help to delineate these populations, with RSGs located in a relatively well-defined region in the near-IR ($J - K$) colour-magnitude diagram (CMD), as discussed by Nikolaev & Weinberg (2000). The near-IR CMD from the WFCAM data is shown in Figure 1.2 and was used to further inform our target selection. Employing the updated CMD criteria from ? – modified for the distance and reddening to NGC 6822 – all of our potential targets from the combined optical and near-IR criteria are (notionally) RSGs.

The combined selection methods yielded 58 candidate RSGs, from which 18 stars were observed with KMOS, as shown in Figure 1.3. The selection of the final targets was defined by the KMOS arm allocation software KARMA (?), where the field centre was selected to maximise the number of allocated arms, with priority given to the brightest targets. Optical spectroscopy of eight of our observed stars, confirming them as RSGs, was presented by ?.

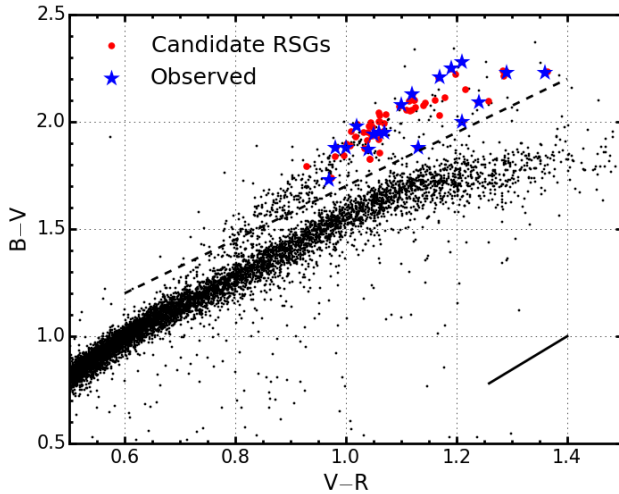


Figure 1.1 Two-colour diagram for stars with good detections in the optical and near-IR photometry in NGC 6822. The black dashed line marks the selection criteria using optical colours, as defined by ?. Red circles mark all stars which satisfied our selection criteria. Large blue stars denote targets observed with KMOS. The solid black line marks the foreground reddening vector for $E(B - V) = 0.22$ (?).

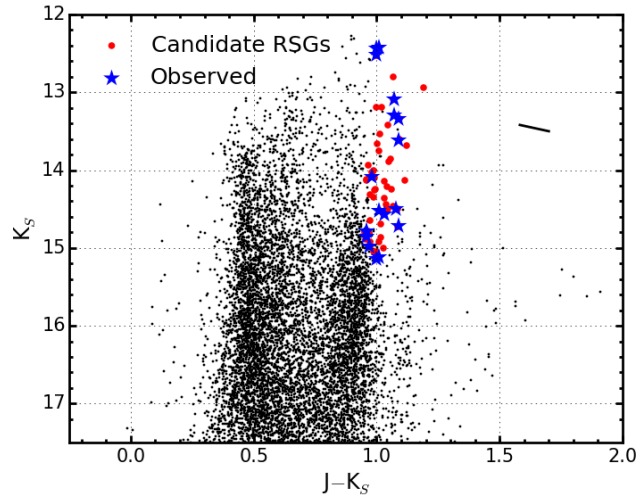


Figure 1.2 Near-IR colour-magnitude diagram (CMD) for stars classified as stellar sources in the optical and near-IR catalogues, plotted using the same symbols as Figure 1.1. This CMD is used to supplement the optical selection. The solid black line marks the foreground reddening vector for $E(B - V) = 0.22$ (?).

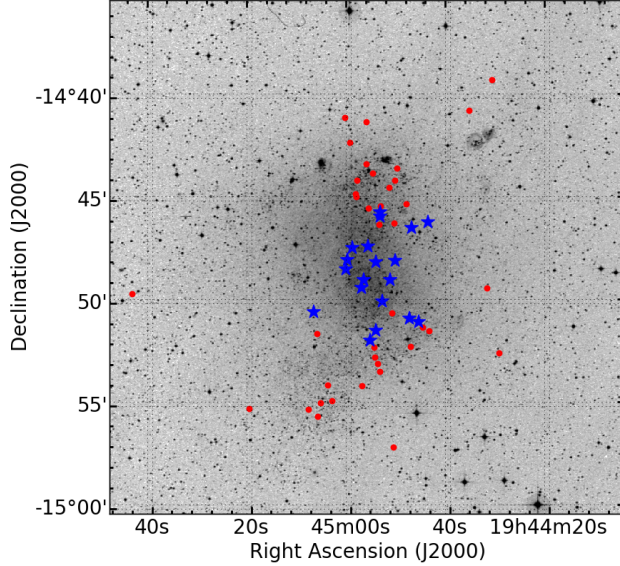


Figure 1.3 Spatial extent of the KMOS targets over a Digital Sky Survey (DSS) image of NGC 6822. Blue stars indicate the locations of the observed red supergiant stars. Red filled circles indicate the positions of red supergiant candidates selected using out photometric criteria (see Section 2.3.1).

1.2.2 KMOS Observations

The observations were obtained as part of the KMOS Science Verification program on 30 June 2013 (PI: Evans, 60.A-9452(A)), with a total exposure time of 2400 s (comprising 8×300 s detector integrations). KMOS has 24 deployable integral-field units (IFUs) each of which covers an area of $2''.8 \times 2''.8$ within a $7''.2$ field-of-view. The 24 IFUs are split into three groups of eight, with the light from each group relayed to different spectrographs. KMOS is described in more detail in Chapter x.x.

Offset sky frames ($0''.5$ to the east) were interleaved between the science observations in an object (O), sky (S) sequence of: O, S, O, O. This observing sequence was chosen over a more standard O S, O sequence to increase time spent on science objects. The observations were performed with the YJ grating (giving coverage from 1.02 to $1.36\mu\text{m}$); estimates of the mean delivered resolving power for each spectrograph (obtained from the KMOS/esorex pipeline for two arc lines) are listed in Table 1.1.

In addition to the science observations, a standard set of KMOS calibration

Table 1.1 Measured velocity resolution and resolving power across each detector.

| Det. | IFUs | Ne $\lambda 1.17700 \mu\text{m}$ | | Ar $\lambda 1.21430 \mu\text{m}$ | |
|------|-------|----------------------------------|----------------|----------------------------------|----------------|
| | | FWHM [km s $^{-1}$] | R | FWHM [km s $^{-1}$] | R |
| 1 | 1-8 | 88.04 ± 2.67 | 3408 ± 103 | 85.45 ± 2.67 | 3511 ± 110 |
| 2 | 9-16 | 82.83 ± 2.48 | 3622 ± 108 | 80.30 ± 3.05 | 3736 ± 142 |
| 3 | 17-24 | 103.23 ± 2.73 | 2906 ± 77 | 101.25 ± 2.99 | 2963 ± 87 |

frames were obtained consisting of dark, flat and arc-lamp calibrations (with flats and arcs taken at six different rotator angles). A telluric standard star was observed with the arms configured in the science positions, i.e. using the *KMOS_spec_cal_stdstarscipatt* template in which the standard star is observed sequentially through all IFUs. The observed standard was HIP97618, with a spectral type of B6 III (Houk & Smith-Moore, 1988).

A summary of the observed targets is given in Table 1.2. A signal-to-noise (S/N) ratio of > 100 per resolution element is required for satisfactory results from this analysis method (see ?). We estimated the S/N ratio of the spectra by comparing the counts in the brightest spatial pixels (within the $1.15\text{-}1.22\mu\text{m}$ region) of each source with the counts in equivalent spatial pixels in the corresponding sky exposures (between the sky lines). The S/N estimated is knowingly an underestimate of the true S/N achieved.

1.3 Data Reduction

The observations were reduced using the recipes provided by the Software Package for Astronomical Reduction with KMOS (SPARK; ?). The standard KMOS/esorex routines were used to calibrate and reconstruct the science and standard-star data cubes as outlined by ?. Sky subtraction was performed using the standard KMOS recipes and telluric correction was performed using two different strategies. Throughout the following analysis all spectra have been extracted from their respective data cubes using a consistent method (i.e. the optimal extractions within the pipeline).

Table 1.2 Summary of VLT-KMOS targets in NGC 6822.

| ID | S/N | α (J2000) | δ (J2000) | B | V | R | J | H | K_s | RV (km s $^{-1}$) | Notes |
|---------------|-----|------------------|------------------|-------|-------|-------|-------|-------|-------|--------------------|---------------------|
| NGC6822-RSG01 | 223 | 19:44:43.81 | -14:46:10.7 | 20.83 | 18.59 | 17.23 | 14.16 | 13.37 | 13.09 | -63.8±3.2 | Sample |
| NGC6822-RSG02 | 120 | 19:44:45.98 | -14:51:02.4 | 20.91 | 18.96 | 17.89 | 15.53 | 14.72 | 14.52 | -60.6±5.5 | Sample |
| NGC6822-RSG03 | 94 | 19:44:47.13 | -14:46:27.1 | 21.30 | 19.41 | 18.41 | 16.13 | 15.35 | 15.12 | -69.8±6.5 | |
| NGC6822-RSG04 | 211 | 19:44:47.81 | -14:50:52.5 | 20.74 | 18.51 | 17.22 | 14.37 | 13.58 | 13.30 | -65.5±4.4 | LM12 (M1), Sample |
| NGC6822-RSG05 | 104 | 19:44:50.54 | -14:48:01.6 | 20.83 | 18.95 | 17.97 | 15.75 | 14.98 | 14.79 | -74.8±5.0 | |
| NGC6822-RSG06 | 105 | 19:44:51.64 | -14:48:58.0 | 21.33 | 19.45 | 18.32 | 15.81 | 14.95 | 14.72 | -65.3±6.0 | |
| NGC6822-RSG07 | 145 | 19:44:53.46 | -14:45:52.6 | 20.36 | 18.43 | 17.38 | 15.06 | 14.30 | 14.08 | -53.8±5.1 | LM12 (M4.5), Sample |
| NGC6822-RSG08 | 103 | 19:44:53.46 | -14:45:40.1 | 20.88 | 19.14 | 18.17 | 15.95 | 15.16 | 14.98 | -51.6±4.1 | LM12 (K5), Sample |
| NGC6822-RSG09 | 201 | 19:44:54.46 | -14:48:06.2 | 20.56 | 18.56 | 17.35 | 14.43 | 13.67 | 13.34 | -47.4±2.1 | LM12 (M1), Sample |
| NGC6822-RSG10 | 302 | 19:44:54.54 | -14:51:27.1 | 19.29 | 17.05 | 15.86 | 13.43 | 12.66 | 12.42 | -75.7±3.5 | LM12 (M0), Sample |
| NGC6822-RSG11 | 327 | 19:44:55.70 | -14:51:55.4 | 19.11 | 16.91 | 15.74 | 13.43 | 12.70 | 12.43 | -59.3±4.0 | LM12 (M0), Sample |
| NGC6822-RSG12 | 100 | 19:44:55.93 | -14:47:19.6 | 21.43 | 19.56 | 18.52 | 16.14 | 15.33 | 15.14 | -39.2±4.6 | LM12 (K5) |
| NGC6822-RSG13 | 106 | 19:44:56.86 | -14:48:58.5 | 21.05 | 19.06 | 18.04 | 15.81 | 15.05 | 14.85 | -55.7±7.4 | |
| NGC6822-RSG14 | 284 | 19:44:57.31 | -14:49:20.2 | 19.69 | 17.41 | 16.20 | 13.52 | 12.76 | 12.52 | -84.2±1.9 | LM12 (M1), Sample |
| NGC6822-RSG15 | 124 | 19:44:59.14 | -14:47:23.9 | 21.30 | 19.17 | 18.05 | 15.58 | 14.74 | 14.50 | -86.9±6.6 | |
| NGC6822-RSG16 | 107 | 19:45:00.24 | -14:47:58.9 | 21.27 | 19.20 | 18.10 | 15.60 | 14.80 | 14.57 | -67.7±3.1 | |
| NGC6822-RSG17 | 167 | 19:45:00.53 | -14:48:26.5 | 20.84 | 18.75 | 17.51 | 14.70 | 13.86 | 13.61 | -64.8±4.2 | Sample |
| NGC6822-RSG18 | 104 | 19:45:06.98 | -14:50:31.1 | 21.06 | 19.12 | 18.06 | 15.74 | 14.94 | 14.78 | -33.8±11.7 | Sample |

Optical data from ?, with typical photometric uncertainty 0.016, 0.006, 0.010 in B , V and R bands respectively. Near-IR data from the UKIRT survey (see ?, for details), with typical errors 0.015, 0.010, 0.012, in J , H and K bands respectively. Targets observed by ? are indicated by 'LM12' in the final column (with their spectral classifications in parentheses). Targets used for abundance analysis are indicated by the comment 'Sample'.

1.3.1 KMOS/esorex pipeline

The KMOS/esorex pipeline performs the initial calibrations by using a set of dark, flat and arc-lamp calibrations. These calibrations are all performed on raw KMOS images which contain 14×14 spectra from each IFU from the three spectrographs. The flat-field calibrations allow one to trace the spatial coordinates of each spectrum on the raw images. This information is then combined with the wavelength calibration information, obtained from the arc-lamp calibrations, to give a $14 \times 14 \times 2056$ 3-D spectrum for each IFU across the detector. A snapshot of the 14×14 spatial pixels is shown in Figure 1.4. When reducing multiple exposures of a single object, this cube is then combined to produce the final data cube.

There are many routines with which to extract spectra from this final data cube. The simplest way to do this is to take the single brightest spectral pixel within the cube and extract a spectrum from that. However, higher signal-to-noise can be achieved by extracting the spectrum from a circular pixel mask centred on the brightest pixel, where each pixel is weighted by the integrated flux in that pixel. However, within each IFU, the resolution of the spectrum varies between spatial pixels. Therefore, in order to combine the spectra more precisely, one must first standardise the resolution across the IFU before combining (Gazak et al., 2015).

1.3.2 Sky Subtraction

Sky subtraction is performed within the pipeline before IFU reconstruction where the science frame is matched with its nearest in time sky frame. Initial inspection of the extracted stellar spectra revealed minor residuals from the sky subtraction process. Reducing these cases with the ‘sky_tweak’ option within the KMOS/esorex reduction pipeline was ineffective to improve the subtraction of these features. Any residual sky features could potentially influence our results by perturbing the continuum placement within the model fits, which is an important aspect of the fitting process (see ??, for more discussion). Thus, pending a more rigorous treatment of the data (e.g. to take into account the changing spectral resolution across the array), we exclude objects showing sky residuals from our analysis. Of the 18 observed targets, 11 were used to derive stellar parameters (as indicated in Table 1.2).

In-house Sky Subtraction

An alternative method of sky subtraction would to subtract the sky from spatial pixels within the object IFU. This is possible as within each IFU the target does not extend over the entire set of spatial pixels as Figure 1.4 demonstrates. Using a collection of these spatial pixels which contain little or no object flux can be a potential method for sky subtraction. Clearly this method has large potential benefits with respect to observing efficiency as less sky exposures would be needed for a given observing run. Theoretically, the sky subtraction from a region which is nearer in space to the object in question is beneficial in two different ways:

- i The sky being subtracted more closely represents the sky background which the object is contaminated with. For comparison, during the sky exposures the telescope is offset by ~ 10 arc-minutes, therefore, this sky exposure samples an intrinsically different atmospheric column when compared to the science exposure. Even though the differences in the sky lines on this spatial scale is small, as the signal originating from the sky is roughly an order of magnitude larger than that of our object, a small sky residual could affect the shape and/or strength of a genuine stellar feature.
- ii The region of the host galaxy which the target object occupies will often contain contaminating flux. By sampling a region of space closer to the position of the target object, the underlying galaxy flux will be more accurately subtracted.

However, an inherent issue with this method of sky subtraction is that one may well remove some of the object flux in this process. Additionally, (as mentioned in 1.3.1) there is known to exist a slight difference in resolution over the spatial extent of the IFU which could make comparisons between spatial pixels complicated. By standardising the resolution across the IFU one can potentially obtain a more reliable sky subtraction at the expense of the resolution of the spectrum.

1.3.3 Telluric Correction

One of the most important stages within the data reduction process for spectroscopic observations from ground-based observatories concerned with measuring

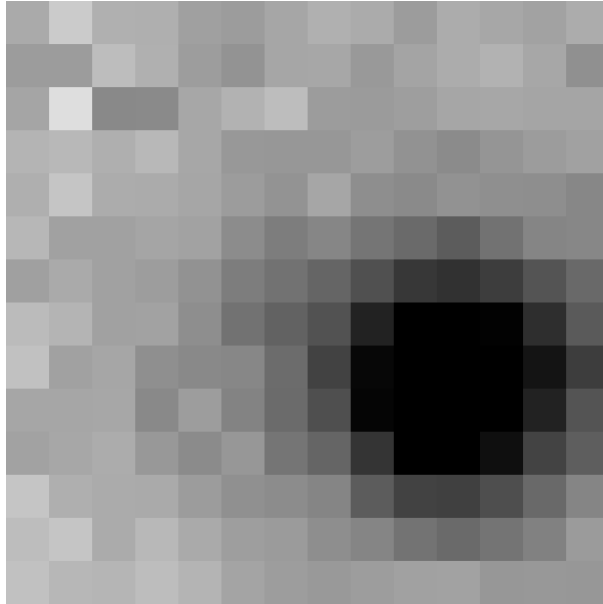


Figure 1.4 *Snapshot of a reconstructed KMOS IFU (at $\lambda = 1.16\mu\text{m}$) containing the science target NGC6822-RSG17. Darker shades indicate higher flux. This image serves to demonstrate that the target objects do not entirely fill the KMOS IFU. This therefore, presents the possibility for using several pixels which do not contain flux from the object in the sky subtraction process.*

absorption, rather than emission, features is the correction for the effects of the Earth’s atmosphere. As starlight passes through the atmosphere it is absorbed and re-emitted by various different molecules. These strong molecular features contaminate and blend genuine stellar features. In order to recover the stellar features a spectrum is derived which contains only the atmospheric absorption features. This spectrum is then used to correct the science spectrum.

Typically, one generates a telluric spectrum by observing an additional star of known spectral type. If the stellar features are well characterised for this spectral type, any additional features are assumed to be owing to the Earth’s atmosphere. The spectral type is usually chosen to minimize the number of stellar features present in the region of interest. In the J -band an A0V star has few lines of note and is therefore a good choice of telluric standard star in this regime. This method of telluric correction is robust and well tested and is the preferred method for many different studies. However, it does have some fairly fundamental limitations which include the fact that it is impossible to sample precisely the same atmospheric column in both the science and telluric observations, as well as the additional time it takes to observe a standard star.

Recently, a tool for telluric correction which does not require standard star observations has been developed and tested on some VLT instruments (?). This package uses atmospheric modelling techniques to derive a telluric spectrum. The package is briefly explained in section 1.3.6, however, see ? for a more thorough description.

1.3.4 Three-arm vs 24 arm Telluric Correction

The default template for telluric observations with KMOS is to observe a standard star in one IFU in each of the three spectrographs. However, there is an alternative template which allows users to observe a standard star in each of the 24 IFUs. This strategy should provide an optimum telluric correction for the KMOS IFUs but reduces observing efficiency.

A comparison between the two methods in the H -band was given by ?, who concluded that using the more efficient three-arm method was suitable for most science purposes. However, an equivalent analysis in the YJ -band was not available. To determine if the more rigorous telluric approach is required for our analysis, we observed a telluric standard star (HIP97618) in each of the 24 IFUs. This gave us the data to investigate both telluric correction methods and to directly compare the results.

We first compared the standard-star spectrum in each IFU with that used by the pipeline routines for the three-arm template in each of the spectrographs. Figure 1.5 shows the differences between the standard-star spectra across the IFUs, where the differences in the YJ -band are comparable to those in the H -band (cf. Fig.7 from ?). The qualitative agreement between the IFUs in our region of interest ($1.16\text{-}1.22\mu\text{m}$) is generally very good.

To quantify the difference the two telluric methods would make to our analysis, we performed the steps described in Section 1.3.5 for both templates. We then used the two sets of reduced science data (reduced with both methods of the telluric correction) to compute stellar parameters for our targets. The results of this comparison are detailed in Section 1.4.1.

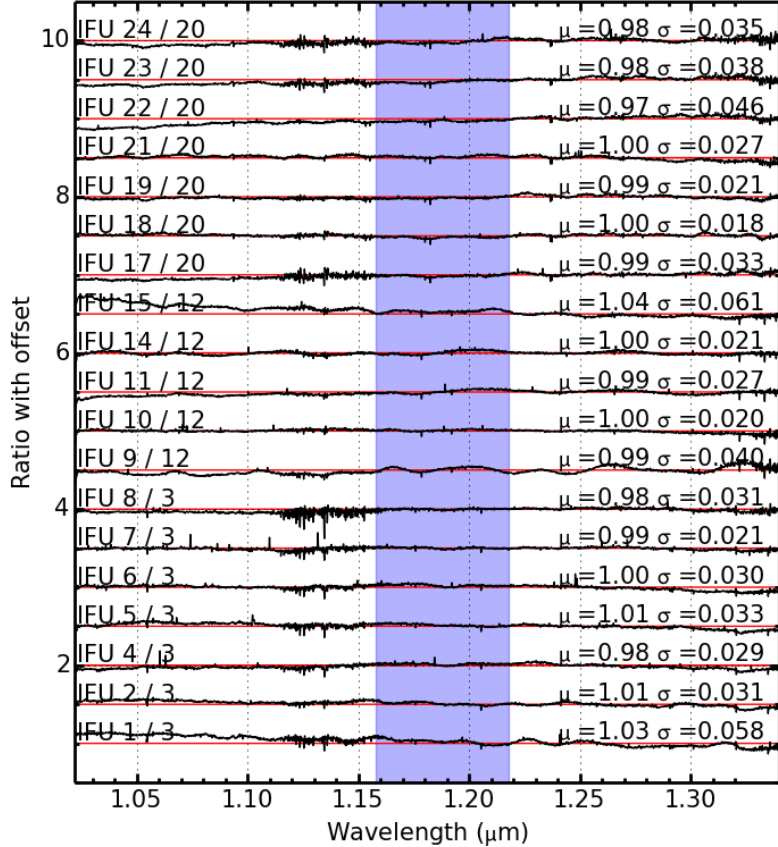


Figure 1.5 Comparison of *J*-band spectra of the same standard star in each IFU. The ratio of each spectrum compared to that from the IFU used in the three-arm telluric method is shown, with their respective mean and standard deviation (μ and σ). Red lines indicate $\mu = 1.0$, $\sigma = 0.0$ for each ratio. The blue shaded area signifies the region used in our analysis, within which, the discrepancies between the IFUs are generally small. This is reflected in the standard deviation values when only considering this region. (IFUs 13 and 16 are omitted as no data were taken with these IFUs.)

1.3.5 Telluric Correction Implementation

To improve the accuracy of the telluric correction, for both methods mentioned above, we implemented additional recipes beyond those of the KMOS/esorex pipeline. These recipes were employed to account for two effects which could potentially degrade the quality of the telluric correction. The first corrects for any potential shift in wavelength between each science spectrum and its associated telluric standard. The most effective way to implement this is to cross-correlate each pair of science and telluric-standard spectra. Any shift between the two is then applied to the telluric standard using a cubic-spline interpolation routine.

The second correction applied is a simple spectral scaling algorithm. This routine corrects for differences in line intensity of the most prominent features common to both the telluric and science spectra. To find the optimal scaling parameter the following formula is used,

$$T_2 = (T_1 + c)/(1 + c), \quad (1.1)$$

where T_2 is the corrected telluric-standard spectrum, T_1 is the initial telluric standard spectrum and c is the scaling parameter.

To determine the required scaling, telluric spectra are computed for $-0.5 < c < 0.5$, in increments of 0.02 (where a perfect value, i.e. no difference in line strength, would be $c = 0$). Each telluric spectrum is used to correct the science data and the standard deviation of the counts across the spectral region is computed for each corrected spectrum. The minimum value of the standard-deviation matrix defines the optimum scaling. For this algorithm, only the region of interest for our analysis is considered (i.e. 1.16-1.22 μm).

The final set of telluric-standard spectra from the KMOS/esorex reductions were modified using these additional routines and were then used to correct the science observations for the effects of the Earth's atmosphere.

1.3.6 MOLECFIT

As an alternative to observing telluric standard stars, a new telluric correction package, MOLECFIT, allows one to calculate a telluric spectrum based on

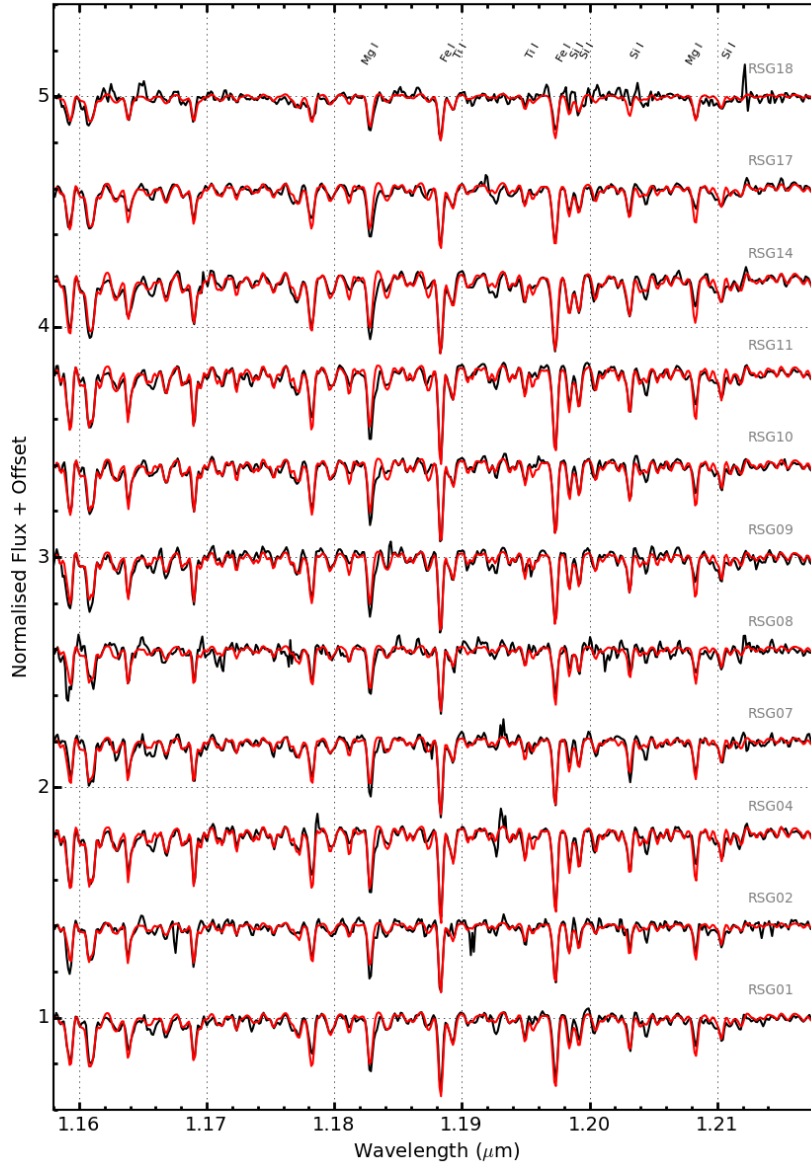


Figure 1.6 KMOS spectra of the NGC 6822 RSGs and their associated best-fit model spectra (black and red lines, respectively). The lines used for the analysis from left-to-right by species are: $Fe\,I\lambda\lambda 1.188285, 1.197305$, $Si\,I\lambda\lambda 1.198419, 1.199157, 1.203151, 1.210353$, $Ti\,I\lambda\lambda 1.189289, 1.194954$. The two strong $Mg\,I$ lines are also labelled, but are not used in the fits (see Section 1.4).

Table 1.3 Cross-correlation shift values and rescaling (c) values.

| Name | 24 AT | | 3 AT | |
|---------------|--------|-------|--------|-------|
| | Shift | c | Shift | c |
| NGC6822-RSG01 | 0.143 | 0.112 | 0.051 | 0.130 |
| NGC6822-RSG02 | 0.135 | 0.140 | 0.184 | 0.216 |
| NGC6822-RSG03 | 0.115 | 0.104 | 0.036 | 0.112 |
| NGC6822-RSG04 | 0.133 | 0.122 | 0.133 | 0.122 |
| NGC6822-RSG05 | 0.054 | 0.198 | -0.017 | 0.206 |
| NGC6822-RSG06 | 0.127 | 0.224 | 0.163 | 0.226 |
| NGC6822-RSG07 | -0.048 | 0.148 | 0.052 | 0.092 |
| NGC6822-RSG08 | 0.062 | 0.180 | 0.062 | 0.180 |
| NGC6822-RSG09 | 0.077 | 0.060 | 0.012 | 0.090 |
| NGC6822-RSG10 | -0.014 | 0.102 | 0.150 | 0.134 |
| NGC6822-RSG11 | 0.067 | 0.134 | 0.060 | 0.110 |
| NGC6822-RSG12 | 0.007 | 0.228 | -0.019 | 0.182 |
| NGC6822-RSG13 | -0.329 | 0.290 | -0.310 | 0.342 |
| NGC6822-RSG14 | -0.464 | 0.138 | -0.021 | 0.258 |
| NGC6822-RSG15 | -0.324 | 0.206 | -0.585 | 0.250 |
| NGC6822-RSG16 | -0.230 | 0.196 | -0.207 | 0.244 |
| NGC6822-RSG17 | -0.192 | 0.160 | -0.192 | 0.160 |
| NGC6822-RSG18 | -0.521 | 0.366 | -0.458 | 0.364 |

atmospheric modelling. Briefly, the software uses a reference atmospheric profile to estimate the true profile for the time and location of the science observation. This model is then used to create a telluric spectrum which can be used to correct the observations.

This software has been shown to work well, on a variety of VLT instruments (?) and has been rigorously tested using X-shooter spectra (?). However, the package has yet to be tested thoroughly on lower-resolution observations such as those from KMOS. Our first tests appear encouraging, however, pending further characterisation of the KMOS data cubes (e.g., small variations in spectral resolving power leading to sky residuals, see Section 1.3.2), I will investigate the potential of the MOLECFIT package with KMOS in the future.

1.3.7 Stellar Radial Velocities

Radial velocities for each target are listed in Table 1.2. The method used here to measure radial velocity values is consistent with that presented in **Chapter x.xx (i.e. as NGC 2100)**. Briefly, radial velocities are calculated using an iterative cross-correlation method. Initially, the accuracy of the wavelength solution provided by the data reduction pipeline is checked against a spectrum of the Earth’s telluric features. Any offset is accounted for and the science spectrum is now assumed to be at “rest” wavelength.

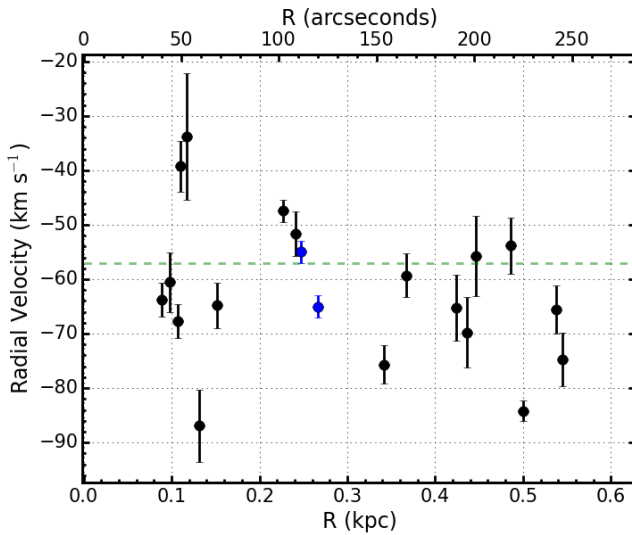


Figure 1.7 Radial velocities of targets shown against their distance from the galaxy centre. The average radial velocity for the sample is $-62 \pm 13 \text{ km s}^{-1}$. The green dashed line indicates HI systemic velocity ($-57 \pm 2 \text{ km s}^{-1}$; ?). The radial velocities of two A-type supergiants from ? are shown in blue.

Once the science spectra are at “rest” wavelength, the spectra are then cross-correlated again an appropriate synthetic RSG model using a large region where stellar features are known to dominate ($1.16 - 1.22\mu\text{m}$). This initial guess is then improved on by selecting seven of the strongest spectral lines in this region and a radial velocity is calculated for each of these lines. The final radial velocity is the mean of these seven strong lines where the error on the measurement is the standard deviation of the measurements normalised by the number of measurements ($\text{err} = \sigma_{rv}/N$).

Radial velocities estimates are shown as a function of distance to the centre of NGC 6822 in Figure 2.4. The average radial velocity for our targets is $-62 \pm 13 \text{ km s}^{-1}$, in good agreement with the systemic radial velocity of the HI disk ($-57 \pm 2 \text{ km s}^{-1}$; ?). Our radial velocities also agree with estimates for the two A-type supergiants from ?. This result confirms that our candidates are NGC 6822 members.

1.4 Results

Stellar parameters (metallicity, effective temperature, surface gravity and microturbulence) have been derived using the *J*-band analysis technique described

Table 1.4 Model grid used for analysis.

| Model Parameter | Min. | Max. | Step size |
|-----------------------|-------|------|-----------|
| T_{eff} (K) | 3400 | 4000 | 100 |
| | 4000 | 4400 | 200 |
| [Z] (dex) | -1.50 | 1.00 | 0.25 |
| $\log g$ (cgs) | -1.0 | 1.0 | 0.5 |
| ξ (km s $^{-1}$) | 1.0 | 6.0 | 1.0 |

by ? and demonstrated by ? and ?. To estimate physical parameters this technique uses a grid of synthetic spectra to fit observational data, in which the models are degraded to the resolution of the observed spectra (Table 1.1). Model atmospheres were generated using the MARCS code (?) where the range of parameters are defined in Table 1.4. The precision of the models is increased by including departures from LTE in some of the strongest Fe, Ti and Si atomic lines (??). The two strong magnesium lines in our diagnostic spectral region are initially excluded from the analysis as these lines are known to be affected strongly by non-LTE effects (see Figure 1.6, where the two Mg I lines are systematically under- and over-estimated, respectively). This is discussed further in Section 1.4.2.

1.4.1 Telluric Comparison

We used these Science Verification data to determine which of the two telluric standard methods is most appropriate for our analysis. Table 1.5 details the stellar parameters estimated for each target using both telluric methods and these parameters are compared in Figure 1.8. The mean difference in the parameters between the two methods is $\langle \Delta\xi \rangle = -0.1 \pm 0.1$, $\Delta[Z] = 0.04 \pm 0.07$, $\langle \Delta \log g \rangle = -0.06 \pm 0.12$ and $\langle \Delta T_{eff} \rangle = -14 \pm 42$. Therefore, for our analysis, there appears to be no significant difference between the two telluric approaches.

1.4.2 The Introduction of Magnesium

Since the publication of Patrick et al. (2015, where the results from this chapter are published), non-LTE corrections have been calculated by ?. Using these results, the model grids have now been updated to include the corrections for non-LTE for the Mg I lines. As an additional calibration to these corrections (to the extensive testing in ?) I have used the updated model grids to re-analyse

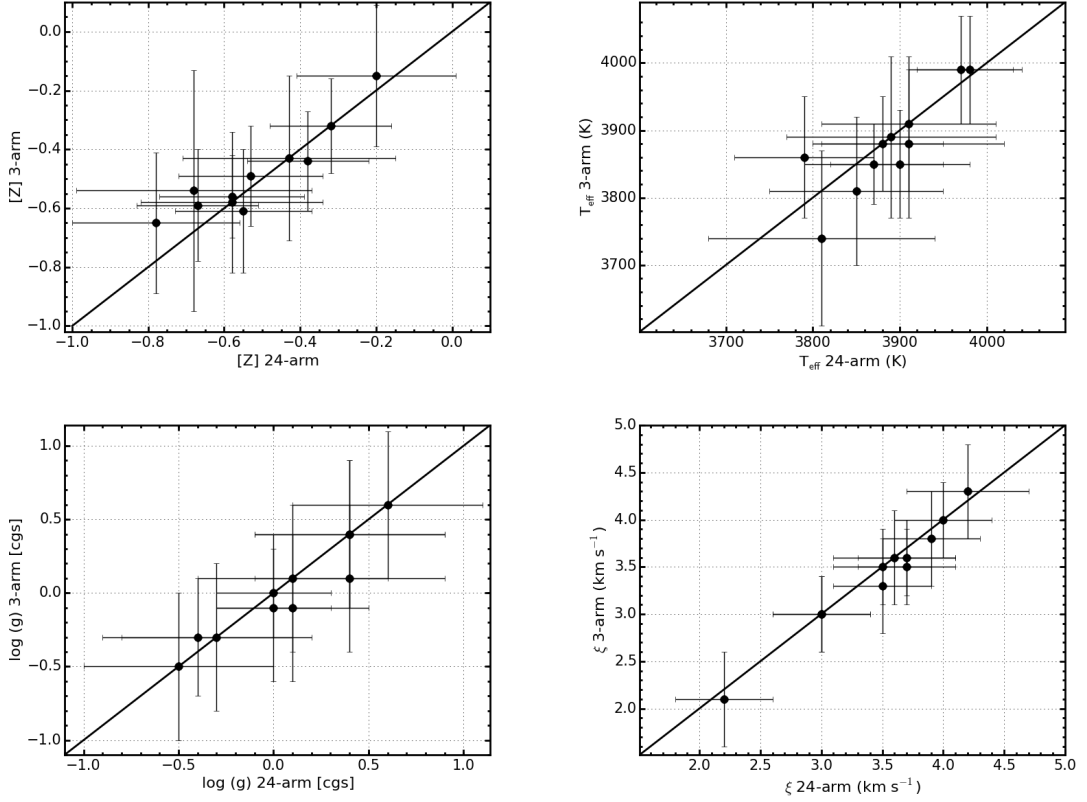


Figure 1.8 Comparison of the model parameters using the two different telluric methods. In each panel, the x -axis represents stellar parameters estimated using the 3 arm telluric method and the y -axis represents those estimated using the 24 arm telluric method. Top left: metallicity ($[Z]$), mean difference $\langle \Delta[Z] \rangle = 0.04 \pm 0.07$. Top right: effective temperature (T_{eff}), mean difference $\langle \Delta T_{\text{eff}} \rangle = -14 \pm 42$. Bottom left: surface gravity ($\log g$), mean difference $\langle \Delta \log g \rangle = -0.06 \pm 0.12$. Bottom right: Microturbulence (ξ), mean difference $\langle \Delta \xi \rangle = -0.1 \pm 0.1$. In all cases, the distributions are statistically consistent with a one-to-one ratio (black lines).

Table 1.5 Fit parameters for reductions using the two different telluric methods.

| Target | IFU | | 24 Arm Telluric | | 3 Arm Telluric | | [Z] |
|---------------|---------------|------------|-----------------------|-----------|----------------|------------|------------|
| | T_{eff} (K) | $\log g$ | ξ (km s $^{-1}$) | [Z] | T_{eff} (K) | $\log g$ | |
| NGC6822-RSG01 | 6 | 3790 ± 80 | -0.0 ± 0.3 | 3.5 ± 0.4 | -0.55 ± 0.18 | 3860 ± 90 | -0.1 ± 0.5 |
| NGC6822-RSG02 | 11 | 3850 ± 100 | 0.4 ± 0.5 | 3.5 ± 0.4 | -0.78 ± 0.22 | 3810 ± 110 | 0.4 ± 0.5 |
| NGC6822-RSG04 | 12 | 3880 ± 70 | 0.0 ± 0.3 | 4.0 ± 0.4 | -0.32 ± 0.16 | 3880 ± 70 | 0.0 ± 0.3 |
| NGC6822-RSG07 | 2 | 3970 ± 60 | 0.4 ± 0.5 | 3.9 ± 0.4 | -0.58 ± 0.19 | 3990 ± 80 | 0.1 ± 0.5 |
| NGC6822-RSG08 | 3 | 3910 ± 100 | 0.6 ± 0.5 | 3.0 ± 0.4 | -0.58 ± 0.24 | 3910 ± 100 | 0.6 ± 0.5 |
| NGC6822-RSG09 | 4 | 3980 ± 60 | 0.1 ± 0.4 | 3.7 ± 0.4 | -0.38 ± 0.16 | 3990 ± 80 | -0.1 ± 0.5 |
| NGC6822-RSG10 | 14 | 3900 ± 80 | -0.3 ± 0.5 | 3.7 ± 0.4 | -0.67 ± 0.16 | 3850 ± 80 | -0.3 ± 0.5 |
| NGC6822-RSG11 | 15 | 3870 ± 80 | -0.4 ± 0.5 | 4.2 ± 0.5 | -0.53 ± 0.19 | 3850 ± 60 | -0.3 ± 0.4 |
| NGC6822-RSG14 | 17 | 3910 ± 110 | -0.5 ± 0.5 | 3.6 ± 0.5 | -0.20 ± 0.21 | 3880 ± 110 | -0.5 ± 0.5 |
| NGC6822-RSG17 | 21 | 3890 ± 120 | 0.1 ± 0.5 | 3.0 ± 0.4 | -0.43 ± 0.28 | 3890 ± 120 | 0.1 ± 0.5 |
| NGC6822-RSG18 | 18 | 3810 ± 130 | 0.4 ± 0.5 | 2.2 ± 0.4 | -0.68 ± 0.31 | 3740 ± 130 | 0.4 ± 0.5 |

the NGC 6822 KMOS spectra. This allows a direct comparison between results including and excluding the Mg I lines.

Figure 1.9 displays the stellar parameters estimated including and excluding the two Mg I lines. This figure shows that there exists no significant difference between the results when the Mg I lines are included. Table 1.6 details the parameters.

For the remainder of this chapter we adopt the updated stellar parameters including the non-LTE effects of Magnesium.

1.4.3 Stellar Parameters and Metallicity

Table 1.6 summarises the estimated stellar parameters. For the remainder of this chapter, when discussing stellar parameters, we adopt those estimated using the 24 arm telluric method including the Mg I lines. (i.e. the results in the left-hand part of Table 1.6.) The average metallicity for our sample of 11 RSGs in NGC 6822 is $\bar{Z} = -0.55 \pm 0.13$. This result is in good agreement with the average metallicity estimated in Patrick et al. (2015, see also Figure 1.10). In addition the results presented here are also in good agreement with results using BSGs (BSGs; ??).

A direct comparison with metallicities from BSGs is legitimate as the method used in the present analysis yield a global metallicity ($[Z]$) which closely resembles the Fe/H ratio estimated in ?. While our $[Z]$ measurements are also affected by Si and Ti, we assume $[Z] = [\text{Fe}/\text{H}]$ for the purposes of our discussion. Likewise, we can compare oxygen abundances (relative to solar) obtained from H II regions as a proxy for $[Z]$ by introducing the solar oxygen abundance $12 + \log(\text{O}/\text{H})_{\odot} = 8.69$ (?) through the relation $[Z] = 12 + \log(\text{O}/\text{H}) - 8.69$. This implicitly assumes that the α/Fe ratio remains Solar in different environments.

As outlined in **Chapter x.x** the RSG and BSG stages are different evolutionary phases within the life cycle of a massive star, while H II regions are the birth clouds which give rise to the youngest stellar population. As the lifetimes of RSGs and BSGs are $< 50\text{Myr}$, their metallicity estimates are also expected to be representative of their birth clouds.

To investigate the spatial distribution of chemical abundances in NGC 6822, in Figure 1.10 we show the metallicities of our RSGs as a function of radial distance from the centre of the galaxy, as well as the results from ? and the indicative

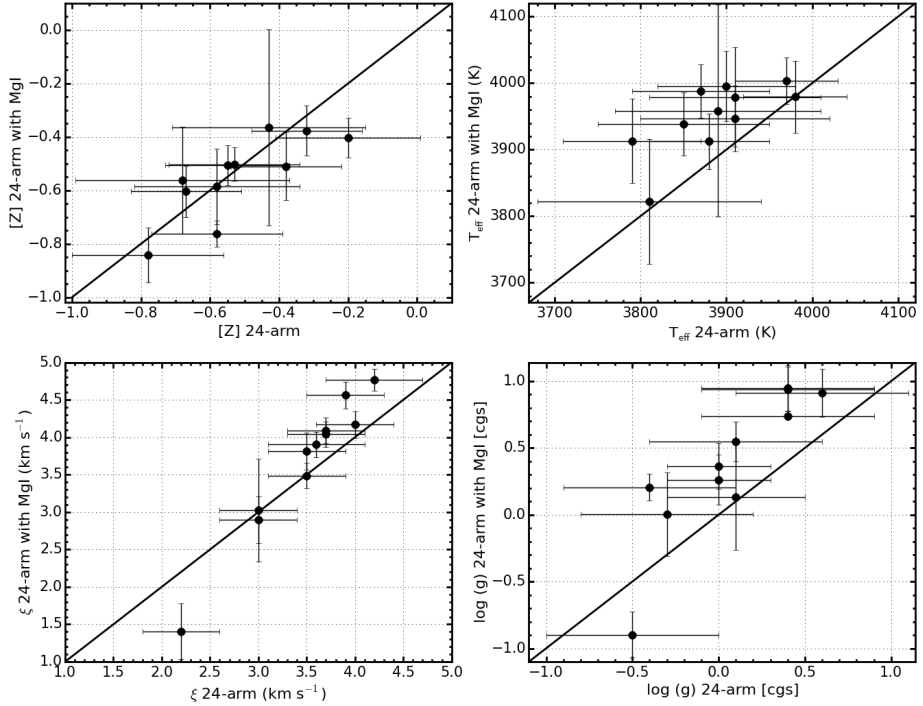


Figure 1.9 Comparison of the model parameters including and excluding MgI lines. In each panel, the x -axis represents stellar parameters estimated excluding the MgI lines and the y -axis represents those estimated including the MgI lines. Top left: metallicity ($[Z]$), mean difference $\langle \Delta[Z] \rangle = 0.03 \pm 0.10$. Top right: effective temperature (T_{eff}), mean difference $\langle \Delta T_{\text{eff}} \rangle = -61 \pm 39$. Bottom left: surface gravity ($\log g$), mean difference $\langle \Delta \log g \rangle = -0.11 \pm 0.37$. Bottom right: Microturbulence (ξ), mean difference $\langle \Delta \xi \rangle = -0.17 \pm 0.38$. In all cases, the distributions are statistically consistent with a one-to-one ratio (black lines).

Table 1.6 Fit parameters including and excluding $Mg\,I$ lines.

| Target | IFU | 24 Arm Telluric without Mg I | | | | 24 Arm Telluric with Mg I | | | |
|---------------|-----|------------------------------|------------|----------|----------------|---------------------------|------------|------------|----------------|
| | | ξ (km s $^{-1}$) | [Z] | $\log g$ | T $_{eff}$ (K) | ξ (km s $^{-1}$) | [Z] | $\log g$ | T $_{eff}$ (K) |
| NGC6822-RSG01 | 6 | 3.5±0.4 | -0.55±0.18 | -0.0±0.3 | 3790±80 | 3.5±0.2 | -0.51±0.07 | 0.26±0.19 | 3910±60 |
| NGC6822-RSG02 | 11 | 3.5±0.4 | -0.78±0.22 | 0.4±0.5 | 3850±100 | 3.8±0.2 | -0.84±0.10 | 0.94±0.17 | 3940±50 |
| NGC6822-RSG04 | 12 | 4.0±0.4 | -0.32±0.16 | 0.0±0.3 | 3880±70 | 4.2±0.2 | -0.38±0.09 | 0.36±0.17 | 3910±40 |
| NGC6822-RSG07 | 2 | 3.9±0.4 | -0.58±0.19 | 0.4±0.5 | 3970±60 | 4.6±0.2 | -0.76±0.05 | 0.74±0.00 | 4000±40 |
| NGC6822-RSG08 | 3 | 3.0±0.4 | -0.58±0.24 | 0.6±0.5 | 3910±100 | 2.9±0.3 | -0.59±0.14 | 0.91±0.18 | 3980±80 |
| NGC6822-RSG09 | 4 | 3.7±0.4 | -0.38±0.16 | 0.1±0.4 | 3980±60 | 4.1±0.2 | -0.51±0.13 | 0.13±0.40 | 3980±50 |
| NGC6822-RSG10 | 14 | 3.7±0.4 | -0.67±0.16 | -0.3±0.5 | 3900±80 | 4.0±0.2 | -0.60±0.10 | 0.00±0.31 | 4000±50 |
| NGC6822-RSG11 | 15 | 4.2±0.5 | -0.53±0.19 | -0.4±0.5 | 3870±80 | 4.8±0.1 | -0.50±0.06 | 0.20±0.10 | 3990±40 |
| NGC6822-RSG14 | 17 | 3.6±0.5 | -0.20±0.21 | -0.5±0.5 | 3910±110 | 3.9±0.2 | -0.40±0.07 | -0.90±0.17 | 3950±50 |
| NGC6822-RSG17 | 21 | 3.0±0.4 | -0.43±0.28 | 0.1±0.5 | 3890±120 | 3.0±0.7 | -0.36±0.37 | 0.55±0.15 | 3960±160 |
| NGC6822-RSG18 | 18 | 2.2±0.4 | -0.68±0.31 | 0.4±0.5 | 3810±130 | 1.4±0.4 | -0.56±0.20 | 0.95±0.17 | 3820±90 |

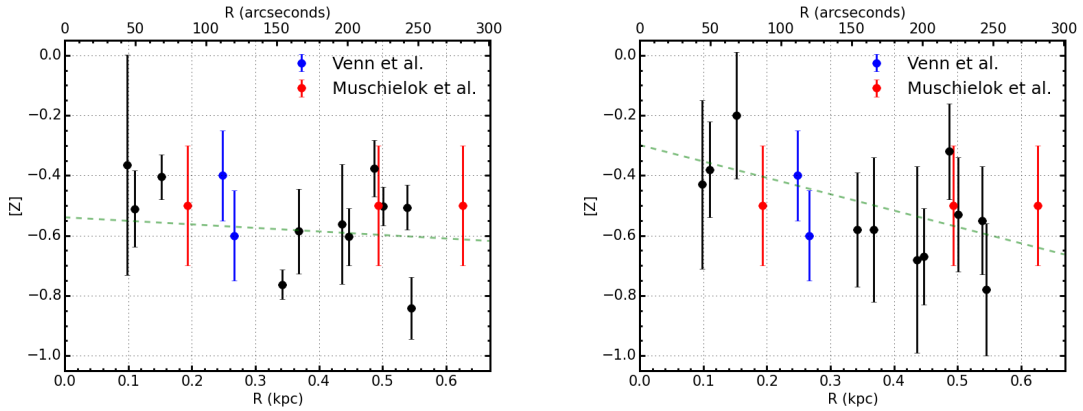


Figure 1.10 Estimated metallicities for 11 RSGs in NGC 6822 shown against their distance from the galaxy centre. The left panel shows the metallicities estimated including MgI lines whereas the right hand panel shows metallicities excluding MgI . Blue and red points show BSG results from ? and ? respectively. The average metallicity is consistent between the two samples and the average including MgI is adopted at $\bar{Z} = -0.55 \pm 0.13$. A least-squares fit to the results excluding MgI (right panel) reveals a low-significance abundance gradient (see text for details). For comparison, $R_{25} = 460$ arcseconds ($= 1.03$ kpc; ?).

estimates from ?.

A least-squares fit to the results from Patrick et al. (2015) reveals a low-significance abundance gradient within the central 1 kpc of NGC 6822 of -0.5 ± 0.4 dex kpc $^{-1}$. In addition, the extrapolated central metallicity from the fit (i.e. at $R = 0$) of $[Z] = -0.30 \pm 0.15$ dex remains consistent with the average metallicity assuming no gradient. However, using the updated stellar parameters the data appears consistent with no gradient (-0.12 ± 0.19 dex kpc $^{-1}$) even though statistically this is a poorer fit to the data.

Figure 1.11 shows the location of our sample in the H–R diagram. Bolometric corrections were computed using the calibration in ?. This figure shows that the temperatures estimated using the J -band method are systematically cooler than the end of the evolutionary models (which terminate at the end of the carbon-burning phase for massive stars) for $Z = 0.002$ from ?. This result is discussed in Section 1.5.2.

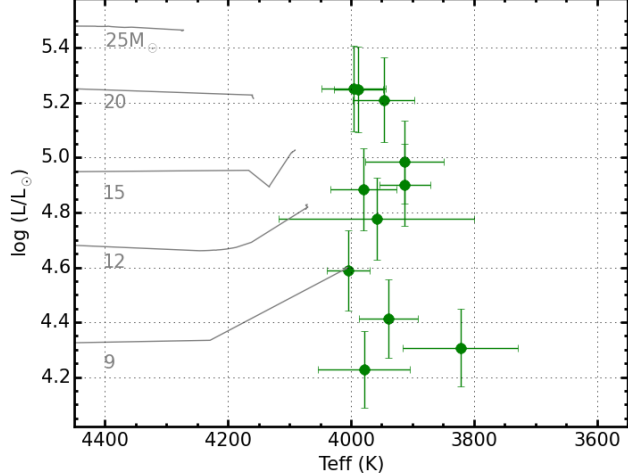


Figure 1.11 *H-R diagram for the 11 RSGs in NGC 6822. Evolutionary tracks including rotation ($v/v_c = 0.4$) for SMC-like metallicity ($Z = 0.002$) are shown in grey, along with their zero-age mass (?). Bolometric corrections are computed using the calibration in ?. We note that compared to the evolutionary tracks, the observed temperatures of NGC 6822 RSGs are systematically cooler. This is discussed in Section 1.5.2.*

1.5 Discussion

1.5.1 Metallicity Measurements

The average metallicity for the sample is $\bar{Z} = -0.55 \pm 0.13$, which agrees well with the results estimated from BSGs (???) and H II regions (?). These results are consistent with no metallicity gradient within NGC 6822.

Using the data from (Patrick et al., 2015, i.e excluding Mg I) there exists a low-significance metallicity gradient within the central 1 kpc of NGC 6822 ($-0.5 \pm 0.4 \text{ dex kpc}^{-1}$ with a $\chi^2_{\text{red}} = 1.16$; see Figure 1.10). The gradient estimated is consistent with the trend reported in ? from their results for the two BSGs which these authors compared with H II regions (?) and two planetary nebulae (?) at larger galactocentric distances. This result is also consistent with the gradient estimated from a sample of 49 local star-forming galaxies (?). Including the results for BSGs from ? in the analysis, gives a consistent gradient ($-0.48 \pm 0.33 \text{ dex kpc}^{-1}$) with an improved $\chi^2_{\text{red}} = 1.06$. Results from ? are not included in the fit as these measurements were qualitative estimates of metallicity.

In contrast, ? used the oxygen abundances from 19 H II regions and found no clear evidence for a metallicity gradient. Using a subset of the highest quality H II region data available, these authors found a gradient of $-0.16 \pm 0.05dex kpc^{-1}$. Including these results into our analysis degrades the fit and changes the estimated gradient significantly ($-0.18 \pm 0.05dex kpc^{-1}$; $\chi^2_{red} = 1.78$). However, when this data is combined with the RSG data including the Mg I lines, a significant gradient is measured ($-0.13 \pm 0.04dex kpc^{-1}$; $\chi^2_{red} = 2.91$). At this point it is not clear whether the indication of a gradient obtained from the RSGs and BSGs is an artefact of the small sample size, or indicates a difference with respect to the H II region study.

There have been a number of studies of the metallicity of the older stellar population in NGC 6822. From spectroscopy of red giant branch (RGB) stars, ? found a mean metallicity of $[Fe/H] = -0.9$ with a reasonably large spread (see their Figure 19). More recently, ? derived metallicities using a population of AGB stars within the central 4 kpc of NGC 6822. They found an average metallicity of $[Fe/H] = -1.29 \pm 0.07 dex$. Likewise, ? used spectra of red giant stars within the central 2 kpc and found an average metallicity of $[Fe/H] = -1.05 \pm 0.49 dex$. We note that none of these studies found any compelling evidence for spatial variations in the stellar metallicities, which is not surprising given that, in disc galaxies, radial migration is thought to smooth out any abundance gradients over time. The stellar populations used for these studies are known to be significantly older than our sample, therefore, owing to the chemical evolution in the time since the birth of the older populations, we expect the measured metallicities to be significantly lower.

The low metallicity of the young stellar population and the interstellar medium (ISM) in NGC 6822 can be understood as a consequence of the fact that it is a relatively gas-rich galaxy with a mass $M_{HI} = 1.45 \times 10^8 M_\odot$ (?) and a total stellar mass of ranging from $M_* = 0.83 - 1.70 \times 10^8 M_\odot$ (??).

The simple closed-box chemical-evolution model relates the metallicity mass fraction $Z(t)$ at any time to the ratio of stellar to gas mass M_*/M_g through

$$Z(t) = \frac{y}{1-R} \ln \left[1 + \frac{M_*(t)}{M_g(t)} \right], \quad (1.2)$$

where y is the fraction of metals per stellar mass produced through stellar nucleosynthesis (the so-called yield) and R is the fraction of stellar mass returned

to the ISM through stellar mass-loss.

According to ?, the ratio $y/(1 - R)$ can be empirically determined from the fact that the metallicity of the young stellar population in the solar neighbourhood is solar, with a mass fraction $Z_\odot = 0.014$ (?). With a stellar-to-gas mass column density of 4.48 in the solar neighbourhood (??) one then obtains $y/(1 - R) = 0.0082 = 0.59Z_\odot$ with an uncertainty of 15 percent dominated by the 0.05 *dex* uncertainty of the metallicity determination of the young population.

Accounting for the presence of helium and metals in the neutral interstellar gas we can turn the observed HI mass in NGC 6822 into a gas mass via $M_g = 1.36 M_{HI}$ and use the simple closed-box model to predict a metallicity of $[Z] = -0.44 - -0.69$, in good agreement with our value obtained from RSG spectroscopy.

As discussed above, the older stellar population of AGB stars has a metallicity roughly 0.8 *dex* lower than the RSGs. In the framework of the simple closed-box model this would correspond to a period in time where the ratio of stellar to gas mass was ~ 0.1 (much lower than the present value of 0.42-0.86). The present star-formation rate of NGC 6822 is $\sim 0.02 M_\odot \text{yr}^{-1}$ (??). At such a high level of star formation it would have taken five Gyr to produce the presently observed stellar mass and to arrive from the average metallicity of the AGB stars to that of the young stellar population (of course, again relying on the simple closed-box model). Evidence suggests that the star-formation rate was substantially lower in the past (??), therefore, the build up of the observed stellar mass would have taken correspondingly longer.

Given the irregularities present in the stellar and gaseous morphology of NGC 6822, this galaxy may not be a good example of a closed-box system, however it is remarkable that the closed-box model reproduces the observed metallicity so closely.

1.5.2 Temperatures of RSGs

Effective temperatures have been estimated for 11 RSGs from our observed sample in NGC 6822. To date, this represents the fourth data set used to estimate stellar parameters in this way and the first with KMOS. The previous three data sets which have been analysed are those of 11 RSGs in PerOB1, a Galactic star cluster (?), nine RSGs in the LMC and 10 RSGs in the SMC (both from ?).

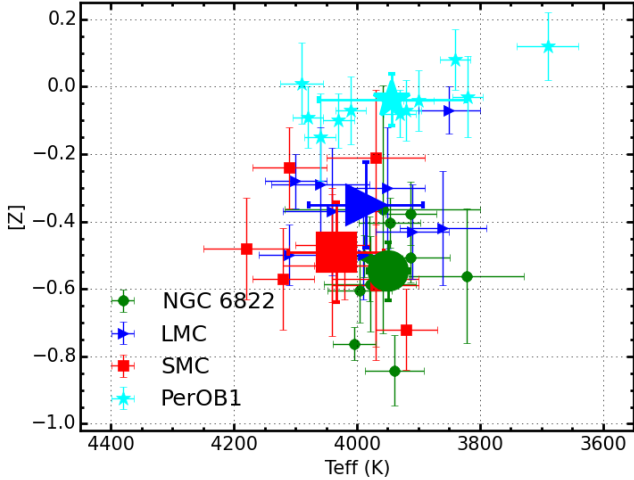


Figure 1.12 Effective temperatures as a function of metallicity for four different data sets using the *J*-band analysis technique. There appears to be no significant variation in the temperatures of RSGs over a range of 0.55 dex. These results are compiled from the LMC, SMC (blue and red points respectively; ?), PerOB1 (a Galactic RSG cluster; cyan; ?) and NGC 6822 (green). Mean values for each data set are shown as enlarged points in the same style and colour. The x-axis is reversed for comparison with Figure 1.13.

These results range from $Z = Z_{\odot}$ in PerOB1 to $Z = 0.3Z_{\odot}$ in the SMC, around 0.5 dex in metallicity.

We compare the effective temperatures estimated in this study to those of the previous results in different environments. Their distribution is shown as a function of metallicity in Figure 1.12. Additionally, Figure 1.13 shows the H–R diagram for the four sets of results. Bolometric corrections to calculate the luminosities for each sample were computed using the calibration in ?.

From these figures, we see no evidence for significant variations in the average temperatures of RSGs with respect to metallicity. This is in contrast to current evolutionary models which display a change of ~ 450 K, for a $M = 15 M_{\odot}$ model, over a range of solar to SMC-like metallicities (??).

For solar metallicity, observations in PerOB1 are in good agreement with the models (see Figure 9 in ?). However, at SMC-like metallicity, the end-points of the models are systematically warmer than the observations. The temperature of the end-points of the evolutionary models of massive stars could depend on the choice of the convective mixing-length parameter (?). That the models produce a higher temperature than observed could imply that the choice of a solar-like

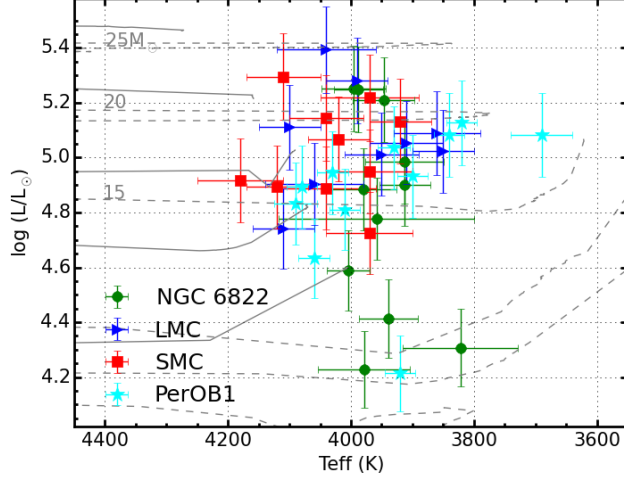


Figure 1.13 *H-R diagram for RSGs in PerOB1 (cyan), LMC (blue), SMC (red) and NGC 6822 (green) which have stellar parameters obtained using the J-band method. This figure shows that there appears to be no significant temperature differences between the four samples. Solid grey lines show SMC-like metallicity evolutionary models including rotation (?). Dashed grey lines show solar metallicity evolutionary models including rotation (?).*

mixing-length parameter does not hold for higher-mass stars at lower metallicity.

Lastly, we note that the average spectral type of RSGs tends towards an earlier spectral type with decreasing metallicity over this range (??). Following the arguments in ? this is not in contradiction to the above results. Spectral types are measured for RSGs using the optical TiO band-heads at $\sim 0.65 \mu\text{m}$, whereas in this study temperatures are estimated using near-IR atomic features (as well as the line-free pseudo-continuum). The strengths of TiO bands are dependent upon metallicity which means that the spectral classification for RSGs at a constant temperature will differ (?). Therefore, although historically spectral type has been used as a proxy for temperature, this assumption does not provide an accurate picture for RSGs.

1.5.3 AGB Contamination

As mentioned in Section 2.3.1, massive AGB stars are potential contaminants to our sample. These stars have similar properties to RSGs and can occupy similar mass ranges as lower-mass RSGs (?), however, their lifetimes are around ~ 25 Myr (?). ? argued for an AGB luminosity limit (owing to the limit on the mass of

the degenerate core) of $M_{bol} \sim -7.1$. Using this maximum luminosity, corrected for the distance to NGC 6822, yields $K = 14.0$. Four of our analysed stars have K -band magnitudes fainter than this limit, but excluding the results for these does not significantly alter any of our conclusions (and arguably, they would still be tracing the young stellar population).

1.6 Conclusions

KMOS spectroscopy of red supergiant stars (RSGs) in NGC 6822 is presented. The data were telluric corrected in two different ways and the standard 3 arm telluric method is shown to work as effectively (in most cases) as the more time expensive 24 arm telluric method. Radial velocities of the targets are measured and are shown to be consistent with previous results in NGC 6822, confirming their extragalactic nature.

Stellar parameters are calculated for 11 RSGs using the J -band analysis method outlined in ?. The average metallicity within NGC 6822 is $\bar{Z} = -0.55 \pm 0.13 \text{ dex}$, consistent with previous abundance studies of young stars. We find an indication of a metallicity gradient within the central 1 kpc, however with a low significance caused by the small size and limited spatial extent of our RSG sample. To conclusively assess the presence of a metallicity gradient among the young population within NGC 6822 a larger systematic study of RSGs is needed.

The chemical abundances of the young and old stellar populations of NGC 6822 are well explained by a simple closed-box chemical evolution model. However, while an interesting result, we note that the closed-box model is unlikely to be a good assumption for this galaxy given its morphology.

The effective temperatures of RSGs in this study are compared to those of all RSGs analysed using the same method. Using results which span 0.55 dex in metallicity (Solar to SMC) within four galaxies, we find no evidence for a systematic variation in average effective temperature with respect to metallicity. This is in contrast with evolutionary models which, for a similar change in metallicity, produces a shift in the temperature of RSGs of up to 450 K. We argue that an observed shift in average spectral type of RSGs over this metallicity range does not imply a shift in average temperature.

Chapter 2

First steps outside the Local Group of Galaxies:Red Supergiants in NGC 55

2.1 Opening Remarks

Owen has kindly helped reconstruct and combine the data sets

2.2 Introduction

NGC 55 is a galaxy located outside of the Local Group of Galaxies within the Sculptor Group at a distance of 1.94 ± 0.03 Mpc (Pietrzyński et al., 2006; Gieren et al., 2008) which, before the emergence of the Araucaria Project (Gieren et al., 2005), had been subject to considerable uncertainty (e.g. Pritchett et al., 1987; van de Steene et al., 2006).

The Sculptor Group is considered to be the closest group of galaxies to our own and offers a fantastic laboratory with which to test theories of stellar and galactic evolution as using an 8-m class telescope, one can resolve individual stars within this group. Association to the Sculptor group however, is a contentious issue. Distance estimates vary to each galaxy, but typically when one references this group the main galaxies associated to this reference are: NGC 55, NGC 247,

NGC 253, NGC 300 and NGC 7793. Where NGC 253 is a large starburst galaxy which is the brightest and most dominant galaxy within this group. In addition to these five large spiral galaxies, there are also numerous (~ 20) dwarf galaxies associated to this group.

By revising distances for nine of these dwarfs Karachentsev et al. (2003) postulated that the Sculptor group was actually more like a filament of galaxies, which intersects the Milky Way group, where NGC 55 and NGC 300 and their surrounding satellite galaxies were potentially not associated with the main group of galaxies in this filament. Regardless of the geometry and association to the Sculptor Group, NGC 55 is the nearest large galaxy to the MW group in the direction of the Sculptor Group.

The morphology of NGC 55 is asymmetric and complicated owing to the high inclination angle (up to 80° ; Hummel, Dettmar & Wielebinski, 1986; Westmeier, Koribalski & Braun, 2013). de Vaucouleurs (1961) classified this galaxy as an LMC-like spiral barred galaxy (SB(s)m) where the bar is seen along the line of sight de Vaucouleurs (1961) prompting various claims that this galaxy is an edge on analogue of the LMC (e.g. Robinson & van Damme, 1964, although not cited heavily – two citations in 50 years – the idea has propagated). Figure 2.1 shows NGC 55 and its complicated morphology where one can see the edge-on disk along the major axis of the galaxy and the brighter central part of the galaxy represents the head of the bar. In addition, to NGC 55 being orientated nearly edge on, extending from the disk-bar system there exists many star formation features such as giant H II regions as well as supergiant filaments and shells which are thought to allow ionising radiation to be transported to the halo where star-formation is currently occurring (Ferguson, Wyse & Gallagher, 1996).

The morphology of NGC 55, as well as its known population of massive hot stars (Castro et al., 2008, 2012), points to a recent history of intense star formation. This is supported by the infrared morphology of NGC 55 which is dominated by young star forming features (Engelbracht et al., 2004, with a star formation rate of $0.22 \text{ M}_\odot \text{yr}^{-1}$) as well as indications from near-IR imaging (Davidge, 2005).

The metal content of NGC 55 is expected to be LMC-like, which is supported by Castro et al. (2012) who measured metallicities of 12 blue supergiants using optical spectroscopy and found a mean metallicity $[Z] = -0.40 \pm 0.13 \text{ dex}$. In addition, Webster & Smith (1983) measure abundances of seven H II regions across



Figure 2.1 *Image of NGC 55 where the edge on disk of the galaxy makes up the major axis and the bright central region represents the head of the bar containing intense star forming regions. Image from the Wide Field Imager on the 2.2-metre MPG/ESO telescope at ESO La Silla Observatory. Credit: ESO, press release.*

the disk of NGC 55 using the strong-line method (as well as four measurements of the auroral “direct” line method) and found a similar LMC-like metallicity.

Even though the hot massive star population of NGC 55 has been explored, there currently exists no confirmed RSGs in NGC 55, although Davidge (2005) note that the near-IR CMDs of fields within the disk of NGC 55 reveal signatures of RSGs. This study represents the first quantitative study of RSGs in NGC 55 and, by measuring metallicities of this population, will provide a crucial test of the metallicity gradient within this galaxy.

In this chapter I describe the observations undertaken in Section 2.3 and highlight the target selection method and its uncertainties. Section ?? details the data reduction process and its complications owing to the poor S/N ratios of the observations. I then present the main results of the chapter in Section 2.5 where I first measure radial velocities for each epoch of the RGSs, confirming their membership to NGC 55, and then go on to measure stellar parameters for each target using the *J*-band analysis technique described in detail in Chapter ???. Section 2.6 presents a discussion of the results and the main conclusions are presented in Section 2.7.

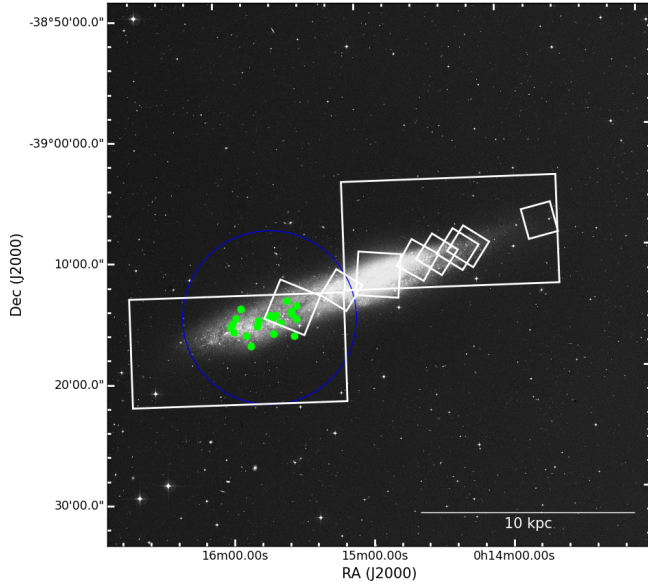


Figure 2.2 DSS image of NGC 55 with KMOS targets overlaid in green and photometric footprints from the Araucaria Project (Gieren et al., 2005) in white rectangles and the ANGST project (Dalcanton et al., 2009) in the smaller white squares.

2.3 Observations

2.3.1 Target Selection

Targets were selected based on the optical photometry from the ACS Nearby Galaxy Survey Treasury (blue; ANGST Dalcanton et al., 2009) project. The optical CMD which is used to select targets is displayed in Figure 2.3, where the RSG candidates are within the black box and the observed targets are highlighted in red. This method of target selection is preferred as a result of the limited extent of near-IR photometry in this area. The ANGST project publicly available photometry for several fields within the disk of NGC 55 that are displayed as small white squares in Figure 2.2, overlaid on a DSS image. In addition to the ANGST HST photometry, ground-based optical photometry is obtained from the Araucaria Project which covers the full spatial extent of NGC 55 (large white rectangles in Figure 2.2).

The selection criteria used in this study makes is based optical $F606 - F814$ colours and $F814$ magnitudes. Owing to their cool temperatures and extreme luminosities RSGs are known to exist in a “plume” at the tip of a structure of cool stars in the $F606 - F814$, $F814$ CMD (e.g. Gazak et al., 2015). Figure 2.3

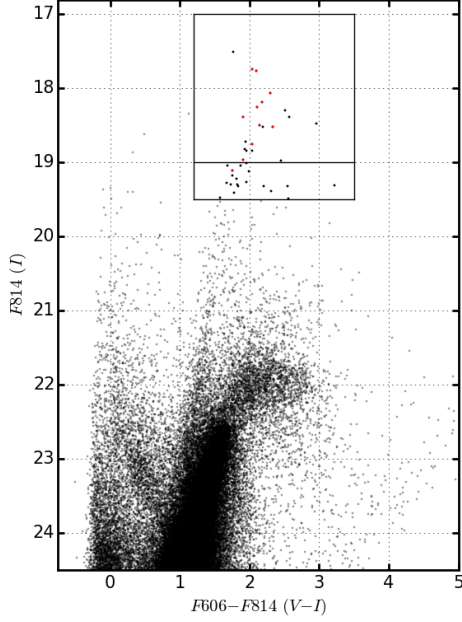


Figure 2.3 *NGC 55 $V - I$ colour-magnitude diagram from the ACS Nearby Galaxy Survey Treasury (ANGST Dalcanton et al., 2009) project. The black box defines the selection criteria for candidate RSGs, which is defined as $17 < F814 < 19$ and $1.2 < F606 - F814 < 3.5$. The lower-panel of the black box defines priority 2 RSG candidates.*

displays this CMD and the region of parameter space where RSG candidates reside is marked with a grey box. This box has the limits $17 < F814 < 19$ and $1.2 < F606 - F814 < 3.5$ following Gazak et al. (2015), where the faint magnitude limit is chosen to select only targets which will have a $S/N = 100$ in the original observing proposal. As with selection criteria in the near-IR, the lower limit of this criteria is contaminated with a population of super-AGB stars which can have luminosities comparable to the faintest RSGs (e.g. Nikolaev & Weinberg, 2000). However, as stated in Chapter ?? these stars are known to have lifetimes similar to the lowest mass RSGs and arguably still trace the young stellar population of this galaxy.

Table 2.1 shows ground- and space-based optical photometry of the KMOS targets along with their radial velocities which confirm many of these targets as NGC 55 RSGs (see section 2.5.1).

Table 2.1 Summary of VLT-KMOS targets in NGC 55.

| ID | S/N | α (J2000) | δ (J2000) | V ^a | I^a | $F606^b$ | $F814^b$ | $\langle rv \rangle$ (km s ⁻¹) | | | Notes |
|-------------|-----|------------------|------------------|----------------|--------|----------|----------|--|------------|----------------------|--------|
| | | | | | | | | 14-09-2013 | 16-10-2013 | 14-09-2014 | |
| NGC55-RSG19 | xx | 00:15:29.190 | -39:14:08.20 | 19.914 | 17.731 | 19.85 | 17.76 | 205±4 | 178±7 | 191±7 | 199±14 |
| NGC55-RSG20 | xx | 00:15:29.520 | -39:15:13.00 | 20.832 | 18.952 | 20.86 | 19.11 | 194±14 | 220±5 | - | 217±10 |
| NGC55-RSG22 | xx | 00:15:30.520 | -39:16:36.70 | 20.406 | 18.589 | - | 18.38 | 95±14 | -41±26 | - | Notes |
| NGC55-RSG24 | xx | 00:15:31.460 | -39:14:46.30 | 20.612 | 18.475 | 20.29 | 18.38 | 186±6 | 194±7 | 146±38 | 192±16 |
| NGC55-RSG25 | xx | 00:15:31.490 | -39:14:32.40 | 20.316 | 18.394 | 20.63 | 18.49 | 204±12 | 217±16 | -376±41 ^c | 151±23 |
| NGC55-RSG26 | xx | 00:15:33.160 | -39:13:42.00 | 20.572 | 17.964 | 20.35 | 18.06 | 174±9 | 173±8 | - | 200±26 |
| NGC55-RSG28 | xx | 00:15:36.160 | -39:15:29.40 | 21.001 | 18.892 | 20.87 | 18.97 | 233±17 | 161±20 | - | 173±1 |
| NGC55-RSG30 | xx | 00:15:38.030 | -39:14:50.20 | 20.867 | 18.730 | 20.79 | 18.75 | 212±10 | 215±10 | -424±21 ^c | 203±41 |
| NGC55-RSG35 | xx | 00:15:39.260 | -39:15:01.70 | 20.007 | 17.872 | 19.78 | 17.73 | 202±3 | 206±4 | 223±13 | 213±2 |
| NGC55-RSG36 | xx | 00:15:39.520 | -39:16:23.10 | 19.915 | 18.462 | - | - | -188±31 | -284±16 | -588±35 | 204±5 |
| NGC55-RSG39 | xx | 00:15:40.260 | -39:15:01.00 | 19.654 | 17.970 | 20.36 | 18.19 | 206±11 | 192±5 | -1±30 ^c | - |
| NGC55-RSG43 | xx | 00:15:40.700 | -39:14:50.20 | 19.957 | 18.183 | 20.36 | 18.25 | -220±20 ^c | 196±5 | 173±17 | 193±14 |
| NGC55-RSG46 | xx | 00:15:41.640 | -39:14:58.80 | 21.591 | 18.441 | 20.85 | 18.52 | 228±5 | 195±6 | -128±18 ^c | 194±9 |
| NGC55-RSG57 | xx | 00:15:45.590 | -39:15:16.40 | 20.010 | 18.220 | - | - | 217±10 | 197±6 | 207±13 | Notes |
| NGC55-RSG58 | xx | 00:15:46.270 | -39:15:43.20 | 20.619 | 18.400 | - | - | 236±8 | 216±3 | 214±21 | Notes |
| NGC55-RSG60 | xx | 00:15:49.180 | -39:17:19.80 | 21.393 | 18.847 | - | - | -73±39 | 26±26 | -533±39 | 218±8 |
| NGC55-RSG65 | xx | 00:15:51.250 | -39:16:26.40 | 19.706 | 17.653 | - | - | 224±5 | 215±4 | 94±37 | - |
| NGC55-RSG67 | xx | 00:15:53.110 | -39:14:13.60 | 19.925 | 18.047 | - | - | 25±24 ^c | 217±6 | 210±8 | Notes |
| NGC55-RSG69 | xx | 00:15:55.280 | -39:15:00.10 | 20.470 | 18.666 | - | - | 231±5 | 195±9 | 177±6 | 193±16 |
| NGC55-RSG70 | xx | 00:15:56.310 | -39:16:08.60 | 22.300 | 18.907 | - | - | 155±12 | 187±9 | 210±13 | Notes |
| NGC55-RSG71 | xx | 00:15:56.900 | -39:15:27.50 | 20.401 | 18.559 | - | - | 197±11 | 214±11 | 320±16 ^c | 180±20 |
| NGC55-RSG73 | xx | 00:15:57.710 | -39:15:41.50 | 20.489 | 18.411 | - | - | 161±7 | 178±6 | -476±42 ^c | 206±12 |
| | | | | | | | | 136±35 | 136±35 | 176±19 | 171±11 |

^a Ground based data from the Araucaria Project Pietrzynski et al. (2006), with typical photometric uncertainty 0.075 and 0.016 in V and I bands respectively.

^b HST ANGST photometry from Dalcanton et al. (2009), with typical errors 0.12, 0.13 in F606 and F814 bands respectively.

^c Value excluded from average for target.

Table 2.2 *NGC 55 observing log.*

| Date | Seeing Conditions (<i>arcsec</i>) | Airmass | Number of Exposures | Notes |
|------------|-------------------------------------|---------|---------------------|----------------------|
| 14-10-2013 | 0''.8–1''.2 | 1.0–1.8 | 6 × 600s | Observed by author |
| 16-10-2013 | 0''.8–1''.2 | 1.0–1.3 | 14 × 600s | Observed by author |
| 14-09-2014 | 0''.4–2''.2 | 1.0–1.9 | 24 × 600s | Back-up observations |
| 15-09-2014 | 1''.1–1''.6 | 1.1–1.5 | 12 × 600s | Back-up observations |

2.4 Observations and Data Reduction

These observations are part of the the KMOS guaranteed time observations (GTO) (ESO ID: 092.B-0088(A)) that was proposed to measure spatial variations in metallicities NGC 55 and NGC 300 both at $d = 1.9\text{Mpc}$. This included three pointings in NGC 55 containing ~ 60 RSG candidates. However, during the observations in October 2013, as a result of poor conditions, only half the requested time on one field in NGC 55 was observed. In order to supplement this partially completed OB, the proposal was re-submitted as a back-up OB for subsequent GTO.

As back-up observations, this OB was observed on two nights in August 2014. Therefore, this OB was observed on four different nights: 14-10-2013, 16-10-2013, 14-09-2014 and 15-10-2014 as detailed by Table 2.2. The observations on each night consisted of science exposures (S) with sky offset exposures (S) interveaved in an O, S, O observing pattern, where each exposure is 600 s.

In addition , on each night a standard set of KMOS calibration files was obtained as well as standard star observations on each night. In October 2013 HIP 3820 (B8 V; Houk, 1978) was observed using the 24-arm telluric template (KMOS_spec_acq_stdstarscipatt). However, on 14-10-2013, this OB was interrupted and several of the IFUs (particularly on detector two) were not observed with the 24-arm recipe: this OB was not repeated.

In August 2014 the 3-arm telluric tempate (KMOS_spec_cal_stdstar) was ob-servsed as opposed to the full 24-arm template. However, on both of these nights both HIP 3820 and HIP 18926 (B3 V; Houk & Smith-Moore, 1988) were observed as a standard star.

The quality of the observations taken on each night varies significantly. The first set of observations (14-09-2013) were taken in excellent conditions where the seeing conditions were stable with good transparency. As one would expect with

Table 2.3 Measured velocity resolution and resolving power across each detector.

| Date | Det. | IFUs | Ne $\lambda 1.17700 \mu\text{m}$ | | Ar $\lambda 1.21430 \mu\text{m}$ | |
|------------|------|-------|----------------------------------|---------------|----------------------------------|----------------|
| | | | FWHM (km s $^{-1}$) | R | FWHM (km s $^{-1}$) | R |
| 14-10-2013 | 1 | 1-8 | 95.48 \pm 2.42 | 3140 \pm 80 | 90.71 \pm 2.09 | 3305 \pm 76 |
| | 2 | 9-16 | 88.67 \pm 1.67 | 3381 \pm 64 | 86.35 \pm 1.84 | 3472 \pm 74 |
| | 3 | 17-24 | 82.89 \pm 1.81 | 3617 \pm 79 | 80.56 \pm 2.11 | 3721 \pm 97 |
| 16-10-2013 | 1 | 1-8 | 95.48 \pm 2.46 | 3140 \pm 81 | 90.78 \pm 2.12 | 3302 \pm 77 |
| | 2 | 9-16 | 88.91 \pm 1.66 | 3371 \pm 63 | 86.30 \pm 1.85 | 3473 \pm 74 |
| | 3 | 17-24 | 82.96 \pm 2.14 | 3612 \pm 76 | 80.77 \pm 2.14 | 3712 \pm 98 |
| 14-09-2015 | 1 | 1-8 | 84.18 \pm 1.93 | 3561 \pm 82 | 81.76 \pm 2.15 | 3667 \pm 96 |
| | 2 | 9-16 | 87.00 \pm 1.69 | 3446 \pm 67 | 84.67 \pm 1.93 | 3541 \pm 81 |
| | 3 | 17-24 | 97.14 \pm 1.88 | 3086 \pm 60 | 94.85 \pm 2.01 | 3161 \pm 67 |
| 15-09-2014 | 1 | 1-8 | 82.55 \pm 1.96 | 3632 \pm 86 | 80.41 \pm 2.30 | 3728 \pm 106 |
| | 2 | 9-16 | 88.08 \pm 1.78 | 3404 \pm 69 | 86.03 \pm 1.96 | 3485 \pm 80 |
| | 3 | 17-24 | 98.04 \pm 1.91 | 3058 \pm 59 | 96.74 \pm 2.05 | 3099 \pm 66 |

back-up observations the conditions were not so idilic. On both nights where this OB was observed as a back-up target, the conditions were varying significantly throughout the night wtih patchy, sometimes significant, cloud coverage.

These differences in the quality of the data and in the actual execution of the observations must all be taken into account when the data is reduced. In addition to differences in the observations arising from the conditions, there are also differences as a result of the time between the observations. Table 2.3 shows the mean measured resolution and resolving power, at the appropriate rotator angles, for each night where the NGC 55 data were taken. This table shows that the resolution can vary significant between each night, particularly on detector three where the mean resolving power changes by a factor of 1/5. Therefore, this must be taking into consideration when combining exposures on different nights. This is solved by using a simple Gaussian filter (as first described in Chapter ??) to degrade the resolution of the spectra to that of the lowest resolution spectrum within the data set. For example, all spectra for a star in IFU 1 would be degraded to a resolution of 3302 before being combined into a master spectrum for the four nights.

Data recuction isn't finalised but the basic steps are not going to change

The observations were reduced using the recipes provided by the Software Package for Astronomical Reduction with KMOS (SPARK; ?). The standard

KMOS/esorex routines were used to calibrate and reconstruct the science and standard-star data cubes as outlined by ? including a correction which corrects for the readout column bias as well as enhancing the bad pixel mask following Turner et al. (in prep.). Sky subtraction was performed using the ESO SKYCORR package (?). SKYCORR is an instrument independent ESO tool that takes an observed spectrum and corresponding sky spectrum and applies a scaling to the sky spectrum in order to more accurately match the sky lines in the observed spectrum. This software is specifically designed for observations at Cerro Paranal and has been shown to be an effective tool for various different science goals (e.g. ?Gazak et al., 2015; ?; ?).

Sky subtraction was performed using the standard KMOS recipes and telluric correction was performed using two different strategies. Throughout the following analysis all spectra have been extracted from their respective data cubes using a consistent method (i.e. the optimal extractions within the pipeline).

- Split recombined sky frames into seeing bins
- combine by including pixel shifts between reconstructed IFUs to ensure all frames are correctly matched
- etc.

Would it be useful to use Skycorr to subtract the sky as in Gazak et al. (2015)

Telluric correction has been performed by combining and reconstructing the telluric standard exposures using the standard pipeline routines. To improve the performance of the telluric correction I use the method described in detail in Chapter ??.

As mentioned above, were multiple standard star OBs for each night of observing. The telluric spectrum used to correct each science spectrum is determined on a star-by-star basis depending upon a visual inspection of the results of the correction.

2.5 Results

2.5.1 Radial Velocities

Radial velocities are measured using the method described first in Chapter ?? where radial velocities are measured using several strong spectral features within the 1.16-1.21 μm region. Each of these spectral features is independently used to measure a radial velocity where the value quoted is the average of these measurements and the uncertainties are defined by the standard deviation of the measurements. This method is known to work well on KMOS stellar spectra Lapenna et al. (2015); Patrick et al. (2015, 2016).

Estimated radial velocities from each KMOS pointing is listed in Table 2.1 alongside the average radial velocity for each target, where any significantly discrepant measurement has been excluded as a result of residuals in the spectrum perturbing the fit (marked by note c in Table 2.1). This is a particular problem on the night of 14-09-2014 where 7/20 velocity measurements were excluded. Uncertainties quoted on the average are the standard deviation of the measurements on each night. Three targets (NGC55-RSG22, NGC55-RSG36 and NGC55-RSG60) have been excluded from this average based on their unreliable radial velocity estimates. Given the significant variability in these measurements on each night, an assessment on membership to NGC 55 is impossible given the current data. Therefore, henceforth, these targets are excluded from the sample.

Comparing the estimated velocities to previous measurements we find good agreement with velocities measured for \sim 200 BSGs in NGC 55 in (Castro et al., 2008) as well as with measurements of the velocity from the H I gas (Puche, Carignan & Wainscoat, 1991). The estimated radial velocities as a function of galactocentric distance is shown in Figure 2.4 where previous measurements are also shown for comparison. The radius at which the surface brightness first reach 25 mag/arcsec² in the *B*-band (R_{25} e.g. Schneider, 2015) is shown for scale ($R_{25} = 16.2 \pm 0.4$ arcmin de Vaucouleurs et al., 1991) We find no evidence for a systematic offset between the measurements of Castro et al. (2008) and those measured in this study.

As the observed data is taken over four different epochs, the variability of each source can be assessed. No clear evidence for variability is found for any target within the observed sample. To assess variability, the variability criteria

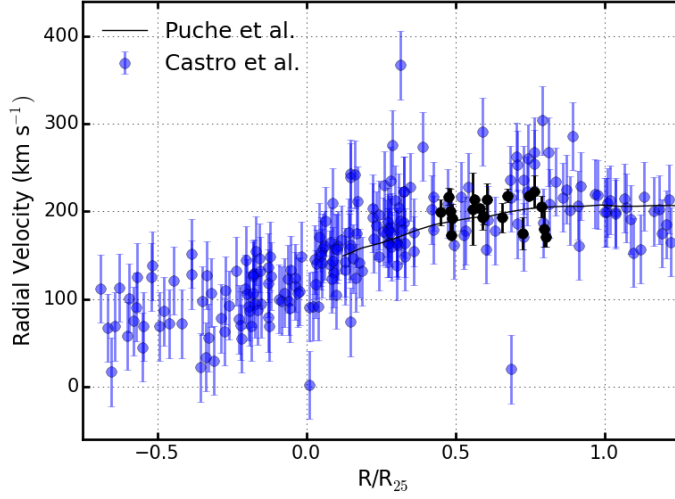


Figure 2.4 Radial velocities for the KMOS RSGs (black points) shown against projected radius from the centre of NGC 55 as defined by the Two Micron All Sky Survey (2MASS; Skrutskie et al., 2006) scaled by $R_{25} = 16.2 \pm 0.4$ arcmin (de Vaucouleurs et al., 1991). Blue points show data for ~ 200 BSGs in NGC 55 from (Castro et al., 2008, ; shown with 50% transparency to highlight densely populated areas) alongside the rotation curve of NGC 55 (black solid line; Puche, Carignan & Wainscoat, 1991).

of (Hénault-Brunet et al., 2012) is employed, i.e.

$$\left| \frac{RV_i - \mu}{\sigma_i} \right| > 4.0, \quad (2.1)$$

where RV_i is the radial velocity with an associated uncertainty σ_i measured on an individual night i and μ is the average radial velocity for the target. Using this criteria on all targets finds that no targets show evidence for variability. This adds strength to the suggestion that observed RSGs are intrinsically single objects as a result of the length of time spent as a RSG in a binary is significantly decreased (see discussion in Chapter ??).

2.5.2 Stellar Parameters

- Comparison to previous results Castro et al. (2012) find average $[Z] = -0.4 \pm 0.13$ dex
- Z Vs. Radius from galaxy centre
- MCMC parameter estimation for the fit

- Extinction values need to be taken into account (especially if I'm estimating luminosities in the I band)

Distance modulus = 26.58 ± 0.11 (Tanaka et al., 2011). Distance modulus = 26.434 ± 0.037 (Gieren et al., 2008)

2.6 Discussion

- Orientation of NGC 55

2.7 Conclusions

Bibliography

- Castro N. et al., 2008, A&A, 485, 41
- Castro N. et al., 2012, A&A, 542, A79
- Dalcanton J. J. et al., 2009, ApJS, 183, 67
- Davidge T. J., 2005, ApJ, 622, 279
- de Vaucouleurs G., 1961, ApJ, 133, 405
- de Vaucouleurs G., de Vaucouleurs A., Corwin, Jr. H. G., Buta R. J., Paturel G., Fouqué P., 1991, Third Reference Catalogue of Bright Galaxies. Volume I: Explanations and references. Volume II: Data for galaxies between 0^h and 12^h . Volume III: Data for galaxies between 12^h and 24^h .
- Engelbracht C. W. et al., 2004, ApJS, 154, 248
- Ferguson A. M. N., Wyse R. F. G., Gallagher J. S., 1996, AJ, 112, 2567
- Gazak J. Z. et al., 2015, ApJ, 805, 182
- Gieren W. et al., 2005, The Messenger, 121, 23
- Gieren W., Pietrzyński G., Soszyński I., Bresolin F., Kudritzki R.-P., Storm J., Minniti D., 2008, ApJ, 672, 266
- Hénault-Brunet V. et al., 2012, A&A, 546, A73
- Houk N., 1978, Michigan catalogue of two-dimensional spectral types for the HD stars
- Houk N., Smith-Moore M., 1988, Michigan Catalogue of Two-dimensional Spectral Types for the HD Stars. Volume 4, Declinations $-26^{\circ}0' - 12^{\circ}0'$.

- Hummel E., Dettmar R.-J., Wielebinski R., 1986, A&A, 166, 97
- Karachentsev I. D. et al., 2003, A&A, 404, 93
- Lapenna E., Origlia L., Mucciarelli A., Lanzoni B., Ferraro F. R., Dalessandro E., Valenti E., Cirasuolo M., 2015, ApJ, 798, 23
- Nikolaev S., Weinberg M. D., 2000, ApJ, 542, 804
- Patrick L. R., Evans C. J., Davies B., Kudritzki R., Hénault-Brunet V., Bastian N., Lapenna E., Bergemann M., 2016, ArXiv e-prints
- Patrick L. R., Evans C. J., Davies B., Kudritzki R.-P., Gazak J. Z., Bergemann M., Plez B., Ferguson A. M. N., 2015, ApJ, 803, 14
- Pietrzyński G. et al., 2006, AJ, 132, 2556
- Pritchett C. J., Schade D., Richer H. B., Crabtree D., Yee H. K. C., 1987, ApJ, 323, 79
- Puche D., Carignan C., Wainscoat R. J., 1991, AJ, 101, 447
- Robinson B. J., van Damme K. J., 1964, in IAU Symposium, Vol. 20, The Galaxy and the Magellanic Clouds, Kerr F. J., ed., p. 276
- Schneider P., 2015, Extragalactic Astronomy and Cosmology: An Introduction
- Skrutskie M. F. et al., 2006, AJ, 131, 1163
- Tanaka M., Chiba M., Komiyama Y., Guhathakurta P., Kalirai J. S., 2011, ApJ, 738, 150
- van de Steene G. C., Jacoby G. H., Praet C., Ciardullo R., Dejonghe H., 2006, A&A, 455, 891
- Webster B. L., Smith M. G., 1983, MNRAS, 204, 743
- Westmeier T., Koribalski B. S., Braun R., 2013, MNRAS, 434, 3511

Appendix A

Accronyns

- 2MASS Two Micron All Sky Survey
BSG Blue supergiant
CCD Colour–colour diagram (not to be confused with CCD: Charged coupled device; not an accroyn used in this thesis)
CCSN Core-collapse supernova
c.g.s Centimeter-gram-second measurement system
CMD Colour–magnitude diagram
DSS Digital sky survey
ESO European southern observatory
FoV Field of view
GRB Gamma-ray burst
GTO Guaranteed time observations
H–R Hertzsprung–Russell
IFS Integral field spectroscopy
IFU Integral field unit
IR Infrared
ISM Interstellar medium
KMOS *K*-band multi-object spectrograph (see Chapter ??)
LBV Luminous blue variable
LMC Large Magellanic cloud
LTE Local thermodynamic equilibrium (see Chapter ??)
MOSFIRE Multi-object spectrometer for infra-red exploration
MS Main sequence
MZR Mass-metallicity relationship

NGC New general catalogue
NS Neutron star
OB Observing block
OSIRIS Optical system for imaging and low-intermediate-resolution integrated spectroscopy
PISN Pair instability supernova
PSF Point spread function
RSG Red supergiant
RSGC Red supergiant cluster
SDSS Sloan digital sky survey
SMC Small magellanic cloud
SN Supernova
SV Science verification
VLT Very large telescope
WLT Wolf-Lundmark-Melotte
WR Wolf-Rayet
YMC Yound massive cluster

Bibliography

- Castro N. et al., 2008, A&A, 485, 41
- Castro N. et al., 2012, A&A, 542, A79
- Dalcanton J. J. et al., 2009, ApJS, 183, 67
- Davidge T. J., 2005, ApJ, 622, 279
- de Vaucouleurs G., 1961, ApJ, 133, 405
- de Vaucouleurs G., de Vaucouleurs A., Corwin, Jr. H. G., Buta R. J., Paturel G., Fouqué P., 1991, Third Reference Catalogue of Bright Galaxies. Volume I: Explanations and references. Volume II: Data for galaxies between 0^h and 12^h . Volume III: Data for galaxies between 12^h and 24^h .
- Engelbracht C. W. et al., 2004, ApJS, 154, 248
- Ferguson A. M. N., Wyse R. F. G., Gallagher J. S., 1996, AJ, 112, 2567
- Gazak J. Z. et al., 2015, ApJ, 805, 182
- Gieren W. et al., 2005, The Messenger, 121, 23
- Gieren W., Pietrzyński G., Soszyński I., Bresolin F., Kudritzki R.-P., Storm J., Minniti D., 2008, ApJ, 672, 266
- Hénault-Brunet V. et al., 2012, A&A, 546, A73
- Houk N., 1978, Michigan catalogue of two-dimensional spectral types for the HD stars
- Houk N., Smith-Moore M., 1988, Michigan Catalogue of Two-dimensional Spectral Types for the HD Stars. Volume 4, Declinations $-26^{\circ}0' - 12^{\circ}0'$.
- Hummel E., Dettmar R.-J., Wielebinski R., 1986, A&A, 166, 97
- Karachentsev I. D. et al., 2003, A&A, 404, 93
- Lapenna E., Origlia L., Mucciarelli A., Lanzoni B., Ferraro F. R., Dalessandro E., Valenti E., Cirasuolo M., 2015, ApJ, 798, 23

- Nikolaev S., Weinberg M. D., 2000, ApJ, 542, 804
- Patrick L. R., Evans C. J., Davies B., Kudritzki R., Hénault-Brunet V., Bastian N., Lapenna E., Bergemann M., 2016, ArXiv e-prints
- Patrick L. R., Evans C. J., Davies B., Kudritzki R.-P., Gazak J. Z., Bergemann M., Plez B., Ferguson A. M. N., 2015, ApJ, 803, 14
- Pietrzynski G. et al., 2006, AJ, 132, 2556
- Pritchett C. J., Schade D., Richer H. B., Crabtree D., Yee H. K. C., 1987, ApJ, 323, 79
- Puche D., Carignan C., Wainscoat R. J., 1991, AJ, 101, 447
- Robinson B. J., van Damme K. J., 1964, in IAU Symposium, Vol. 20, The Galaxy and the Magellanic Clouds, Kerr F. J., ed., p. 276
- Schneider P., 2015, Extragalactic Astronomy and Cosmology: An Introduction
- Skrutskie M. F. et al., 2006, AJ, 131, 1163
- Tanaka M., Chiba M., Komiyama Y., Guhathakurta P., Kalirai J. S., 2011, ApJ, 738, 150
- van de Steene G. C., Jacoby G. H., Praet C., Ciardullo R., Dejonghe H., 2006, A&A, 455, 891
- Webster B. L., Smith M. G., 1983, MNRAS, 204, 743
- Westmeier T., Koribalski B. S., Braun R., 2013, MNRAS, 434, 3511